Determining the Optimal Orientation of Orthotropic Material for Maximizing Frequency Band Gaps

by

Dane Haystead

A thesis submitted in conformity with the requirements
for the degree of Masters of Applied Science
Graduate Department of Aerospace Science and Engineering
University of Toronto

Abstract

Determining the Optimal Orientation of Orthotropic Material for Maximizing Frequency Band Gaps

Dane Haystead

Masters of Applied Science

Graduate Department of Aerospace Science and Engineering

University of Toronto

2012

As the use of carbon fiber reinforced polymers (CFRP) increases in aerospace structures it is important to use this material in an efficient manner such that both the weight and cost of the structure are minimized while maintaining its performance. To combat undesirable vibrational characteristics of a structure an optimization program was developed which takes advantage of the orthotropic nature of composite materials to maximize eigenfrequency bandgaps. The results from the optimization process were then fabricated and subjected to modal testing. The experiments show that local fiber angle optimization is a valid method for modifying the natural frequencies of a structure with the theoretical results generally predicting the performance of the optimized composite plates.

Acknowledgements

First and foremost I would like to thank my advisor, Dr. Craig Steeves, for all of his support and time over the last two years. He allowed me to work at my own pace and always provided valuable insight.

I would also like to thank my colleagues Richard Lee, Collins Ogundipe, and Bryan Wright for always being available to bounce questions off of and for their help in the lab.

Finally, I would like to thank my parents for their continued support in my pursuit of higher education.

Contents

List of Tables

List of Figures

Chapter 1

Introduction

As the use of carbon fiber reinforced polymers (CFRP) increases in aerospace structures it is important to use this material in an efficient manner such that both the weight and cost of the structure are minimized while maintaining its performance. In some cases these structures may have undesirable vibrational characteristics while also being geometrically constrained, creating a unique problem. One possible solution is to take advantage of the orthotropic properties of composite materials and use them to modify the vibrational characteristics while maintaining the overall geometry of the part. The goal of the research presented in this thesis is to develop a method to optimize the fiber orientations throughout thin rectangular composite plates for the maximization of specific eigenfrequencies and eigenfrequency bandgaps.

Fiber reinforced polymers are popular in the aerospace industry due to their high strength to weight ratio and the ever increasing demands on aircraft performance. Composite structures are fabricated by laying up many layers of fibers (either woven or unwoven) into the desired final shape, bonding them together with resin then curing the part. The final properties of a composite structure can depend on several factors of the construction, such as orientation of orthotropic plies, ply thickness, stacking sequence, and material properties of both the reinforcement and matrix (resin). This high degree of

variablility can be taken advantage of to provide an optimal solution for a given scenario, and this can be accomplished using structural optimization.

Structural optimization can take many forms, from shape optimization where, for example, the dimensions of the cross-section of trusses in a structure are optimized to minimize bending stress, to topology optimization, where the layout of material in a design domain is optimized for minimum compliance under the given loads and boundary conditions. While there are many different uses for structural optimization, the general process for finding the optimal design follows the same method.

Topology optimization is a method for determining the optimal layout of material in a specified design domain which satisfies a set of loading and boundary conditions and produces a final product that meets all of the specified requirements. It is a very useful tool in industries where the efficient use of material (reducing weight) is important, such as the aerospace and automotive industries. Typically it is used to determine the optimal layout of material in a structure so that the compliance of the structure is minimized while a constraint on mass is satisfied [15], but it can be can also be applied to wide variety of scenarios such as compliant mechanisms for microelectromechanical devices[18], smart materials [16][17], and maximizing eigenfrequencies and frequency band gaps [10][12]. Optimization of orthotropic material orientation has many similarities with topology optimization; they both are based on a discretized domain where the material properties of the elements are dependent upon the design variables, they share many of the same objective functions, and they both are methods which attempt to determine the most efficient use of material.

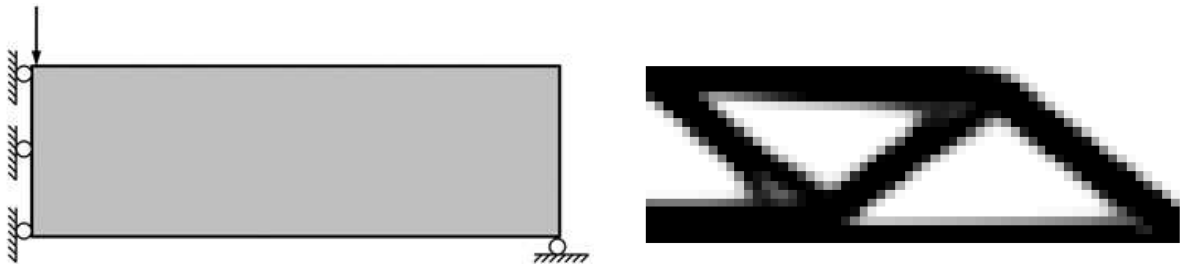

(a) MBB beam domain (b) Optimized topology of MBB beam

Figure 1.1: MBB beam before and after topology optimization

The design variable is major difference between the two. Topology optimization uses the material density of the elements, while fiber angle optimziation uses the angle of the principal material direction. As stated earlier, the goal of both is to find the most efficient use of material under the given conditions, and in the case of fiber angle optimization, this means getting the most benefit from the from the fibers at every point throughout the structure. Having fibers oriented incorrectly can be considered an inefficient use of resources and therefore a waste.

The objective of the thesis is to develop a gradient-based optimization method to determine the optimal orientation of orthotropic material to maximize frequency band gaps in a structure. The optimization method will then be applied to composite laminated plates and the final optimized designs will be fabricated and tested. The next chapter will provide background information on the mathematical methods used to model the behaviour of structures composed of orthotropic material as well as the optimization process used to maximize the frequency band gaps of the composite structures. Chapter three applies these methods to laminated composite plates under various boundary conditions and the optimized fiber orientations are discussed. In Chapter four the results from the optimzation are verified using commercial software and then compared to the results from the modal analysis of the optimized physical specimens. The conclusions and recommendations of the thesis are provided in Chapter five.

Chapter 2

Background

2.1 Finite Element Formulation

To determine the vibrational characteristics of the laminated composite plate with variable fiber angles, the finite element method is used. The plate is discretized as a set of 4-noded plate elements, with each element having its own fiber angle. The vibrational characteristics are determined by solving for the non-trivial solution to the generalized eigenproblem, which is a function of the stiffness and mass matrices, K and M, respectively.

$$K\phi_i = \lambda_i M\phi_i \tag{2.1}$$

The other values in the generalized eigenproblem are λ_i, the eigenvalue, and ϕ_i, the eigenvector. The eigenenfrequency (natural frequency), ω_i, is the sqaure root of the eigenvalue:

$$\omega_i = \sqrt{\lambda_i} \tag{2.2}$$

The generalized eigenproblem can then be simplified to:

$$(K - \omega_i^2 M)\phi_i = 0 \tag{2.3}$$

The K and M matrices are dependent on the properties of the elements used in the discretization of the plate. The optimization of fiber angles was performed separately on two different plate element formulations. Fiber angles were first optimized using 4-noded orthotropic plate elements which model a single ply. The second type of plate element used takes into account the fiber angles of all the orthotropic plies to produce an approximation of a laminated composite plate where the properties of the elements are calculated using First Order Shear Deformation Theory (FSDT), which is an extension of Composite Laminate Theory (CLT) [9][14]. This finite element formulation will be discussed further in Section 2.1.1.

A material is orthotropic when is has three orthogonal planes of symmetry; in the case of a unidirectional lamina, the material symmetry planes are parallel and transverse to the fiber directions. A two-dimensional representation of a unidirectional fiber element can be seen in Figure 2.1.

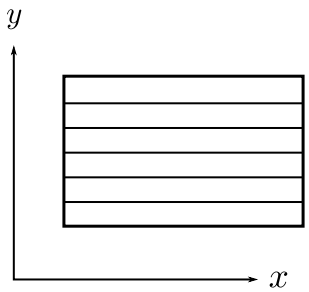

Figure 2.1: Unidirectional fiber element with fibers aligned parallel to the x-axis

Hooke's Law for an anisotropic material can be written (in contracted form) as

$$\sigma_i = C_{ij}\epsilon_j, \tag{2.4}$$

where σ_i are the stress components and ϵ_j are the strain components, while C_{ij} are the material coefficients [14][11]. For orthotropic materials, the number of material coefficients can be reduced from 21 to 9. This results in Equation (2.5).

$$\begin{Bmatrix} \sigma_1 \\ \sigma_2 \\ \sigma_3 \\ \tau_{23} \\ \tau_{31} \\ \tau_{12} \end{Bmatrix} = \begin{bmatrix} C_{11} & C_{12} & C_{13} & & & \\ C_{12} & C_{22} & C_{23} & & & \\ C_{13} & C_{23} & C_{33} & & & \\ & & & C_{44} & & \\ & & & & C_{55} & \\ & & & & & C_{66} \end{bmatrix} \begin{Bmatrix} \epsilon_1 \\ \epsilon_2 \\ \epsilon_3 \\ \gamma_{23} \\ \gamma_{31} \\ \gamma_{12} \end{Bmatrix} \tag{2.5}$$

Laminated composite plates are thin and therefore in a plane state of stress and the transverse normal stress, σ_3, can be neglected. The stress-strain relations in this state are referred to as the plane-stress constitutive relations, and they are written as

$$\begin{Bmatrix} \sigma_1 \\ \sigma_2 \\ \sigma_6 \end{Bmatrix} = \begin{bmatrix} Q_{11} & Q_{12} & 0 \\ Q_{12} & Q_{22} & 0 \\ 0 & 0 & Q_{66} \end{bmatrix} \begin{Bmatrix} \epsilon_1 \\ \epsilon_2 \\ \epsilon_6 \end{Bmatrix}, \tag{2.6}$$

and

$$\begin{Bmatrix} \sigma_4 \\ \sigma_5 \end{Bmatrix} = \begin{bmatrix} Q_{44} & 0 \\ 0 & Q_{55} \end{bmatrix} \begin{Bmatrix} \epsilon_4 \\ \epsilon_5 \end{Bmatrix}, \tag{2.7}$$

where Q_{ij} are the plane stress reduced stiffnesses. When multiple lamina are present, the (k) notation is added to denote the ply that the plane stress-reduced stiffness belongs to. The $Q_{ij}^{(k)}$ values are calculated with the following equations:

$$Q_{11}^{(k)} = \frac{E_1^{(k)}}{1 - \nu_{12}^{(k)}\nu_{21}^{(k)}}, \tag{2.8}$$

$$Q_{12}^{(k)} = \frac{\nu_{12}^{(k)}E_2^{(k)}}{1 - \nu_{12}^{(k)}\nu_{21}^{(k)}}, \tag{2.9}$$

$$Q_{22}^{(k)} = \frac{E_2^{(k)}}{1 - \nu_{12}^{(k)}\nu_{21}^{(k)}}, \tag{2.10}$$

$$Q_{44}^{(k)} = G_{23}^{(k)}, \tag{2.11}$$

$$Q_{55}^{(k)} = G_{13}^{(k)}, \tag{2.12}$$

$$Q_{66}^{(k)} = G_{12}^{(k)}, \tag{2.13}$$

where

$$\nu_{21} = \frac{\nu_{12}E_2}{E_1} \tag{2.14}$$

When the local coordinates of the orthotropic material are not aligned with the global coordinates, as shown in Figure 2.2, the local material coefficients are multiplied by transformation matrices to calculate the global material coefficients, as seen in Equation (2.15).

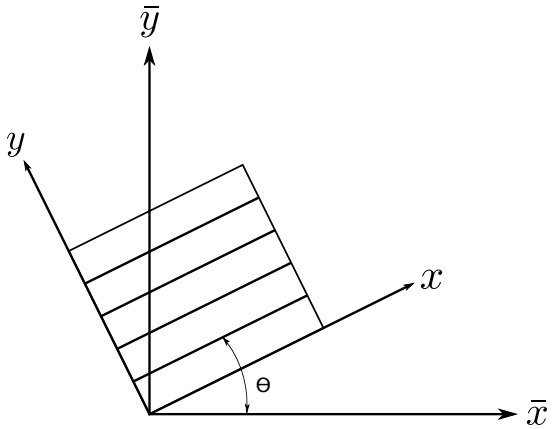

Figure 2.2: Rotated unidirectional ply

$$[\bar{C}] = [T][C][T]^T \tag{2.15}$$

where

$$[T] = \begin{bmatrix} \cos^2\theta & \sin^2\theta & 0 & 0 & 0 & -\sin 2\theta \\ \sin^2\theta & \cos^2\theta & 0 & 0 & 0 & \sin 2\theta \\ 0 & 0 & 1 & 0 & 0 & 0 \\ 0 & 0 & 0 & \cos\theta & \sin\theta & 0 \\ 0 & 0 & 0 & -\sin\theta & \cos\theta & 0 \\ \sin\theta\cos\theta & -\sin\theta\cos\theta & 0 & 0 & 0 & \cos^2\theta - \sin^2\theta \end{bmatrix}, \tag{2.16}$$

and where θ is the angle of the orthotropic material (fiber angle). This results in transformed stress-strain relations for a lamina in a plane state of stress, which are shown in Equations (2.17) and (2.18).

$$\begin{Bmatrix} \sigma_{xx} \\ \sigma_{yy} \\ \sigma_{xy} \end{Bmatrix} = \begin{bmatrix} \bar{Q}_{11} & \bar{Q}_{12} & \bar{Q}_{13} \\ \bar{Q}_{12} & \bar{Q}_{22} & \bar{Q}_{23} \\ \bar{Q}_{13} & \bar{Q}_{23} & \bar{Q}_{66} \end{bmatrix} \begin{Bmatrix} \epsilon_{xx} \\ \epsilon_{yy} \\ \gamma_{xy} \end{Bmatrix}, \tag{2.17}$$

$$\begin{Bmatrix} \sigma_{yz} \\ \sigma_{xz} \end{Bmatrix} = \begin{bmatrix} \bar{Q}_{44} & \bar{Q}_{45} \\ \bar{Q}_{45} & \bar{Q}_{55} \end{bmatrix} \begin{Bmatrix} \gamma_{yz} \\ \gamma_{xz} \end{Bmatrix}, \tag{2.18}$$

$\bar{Q}_{ij}$ are the transformed plane stress-reduced stiffness, and they are calculated with the following equations:

$$\bar{Q}_{11} = Q_{11}\cos^4\theta + 2(Q_{12} + 2Q_{66})\sin^2\theta\cos^2\theta + Q_{22}\sin^4\theta \tag{2.19}$$

$$\bar{Q}_{12} = (Q_{11} + Q_{22} - 4Q_{66})\sin^2\theta\cos^2\theta + Q_{12}(\sin^4\theta + \cos^4\theta) \tag{2.20}$$

$$\bar{Q}_{22} = Q_{11}\sin^4\theta + 2(Q_{12} + 2Q_{66})\sin^2\theta\cos^2\theta + Q_{22}\cos^4\theta \tag{2.21}$$

$$\bar{Q}_{16} = (Q_{11} - Q_{12} - 2Q_{66})\sin\theta\cos^3\theta + (Q_{12} - Q_{22} + 2Q_{66})\sin^3\theta\cos\theta \tag{2.22}$$

$$\bar{Q}_{26} = (Q_{11} - Q_{12} - 2Q_{66})\sin^3\theta\cos\theta + (Q_{12} - Q_{22} + 2Q_{66})\sin\theta\cos^3\theta \tag{2.23}$$

$$\bar{Q}_{66} = (Q_{11} + Q_{22} - 2Q_{12} - 2Q_{66})\sin^2\theta\cos^2\theta + Q_{66}(\sin^4\theta + \cos^4\theta) \tag{2.24}$$

$$\bar{Q}_{44} = Q_{44}\cos^2\theta + Q_{55}\sin^2\theta \tag{2.25}$$

$$\bar{Q}_{45} = (Q_{55} - Q_{44})\cos\theta\sin\theta \tag{2.26}$$

$$\bar{Q}_{55} = Q_{55}\cos^2\theta + Q_{44}\sin^2\theta \tag{2.27}$$

2.1.1 Composite Laminates

As mentioned earlier, FSDT is an extension of CLT, which itself is an extension of Kirchoff plate theory applied to composite plates. Specifically, FSDT includes transverse shear strains, whereas CLT does not. Both FSDT and CLT belong to a group of theories called Equavalent Single Layer theories (ESL), which assumes the laminated plate is a single layer with complex constitutive behaviour. This is one of three major approaches for performing analyses of laminated plates; the others being: 3-D elasticity theories and Multiple model methods.

To approximate multiple plies as an equivalent single layer three stiffness matrices are calculated as a function of the transformed plane stress-reduced stiffnesses, $\bar{Q}_{ij}$, and the ply thicknesses. These matrices are: A_{ij}, the extensional stiffnesses, D_{ij}, the bending stiffnesses, and B_{ij}, the bending-extensional coupling stiffnesses. They are calculated using Equations (2.28-2.30), where the z_k values are calculated based on the ply notation

scheme in Figure 2.3.

$$A_{ij} = \sum_{k=1}^{N} \bar{Q}_{ij}^{(k)}(z_{k+1} - z_k), \tag{2.28}$$

$$B_{ij} = \frac{1}{2}\sum_{k=1}^{N} \bar{Q}_{ij}^{(k)}(z_{k+1}^2 - z_k^2), \tag{2.29}$$

$$D_{ij} = \frac{1}{3}\sum_{k=1}^{N} \bar{Q}_{ij}^{(k)}(z_{k+1}^3 - z_k^3), \tag{2.30}$$

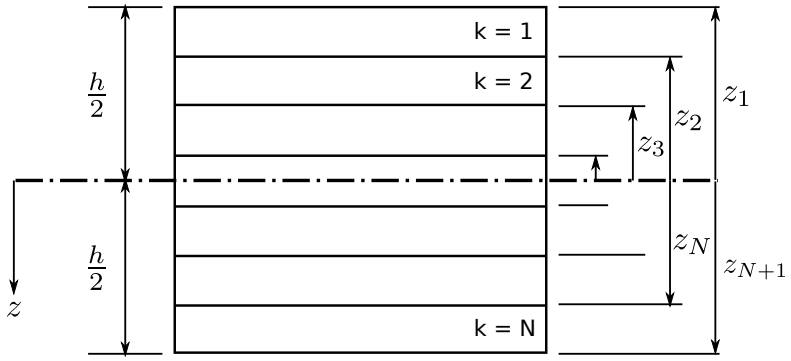

Figure 2.3: The method and notation used for calculating the ply thickness values, z_k, used in the A, B, and D matrix calculations

The stiffness matrices are calculated for each element in the finite element formulation. These matrices are then used to calculate the various membrane, bending, and shear elemental stiffness matrices which are then summed to produce the overall elemental stiffness matrix $[K]^{(e)}$, as shown in Equation (2.31).

$$K^{(e)} = K_{mm}^{(e)} + K_{mb}^{(e)} + K_{bm}^{(e)} + K_{bb}^{(e)} + K_{ss}^{(e)} \tag{2.31}$$

The components of the elemental stiffness matrix are the $K_{mm}^{(e)}$, the membrane portion of the stiffness matrix, $K_{mb}^{(e)}$ and $K_{bm}^{(e)}$, the membrane-bending coupling components, $K_{bb}^{(e)}$,

the bending component, and lastly $K_{ss}^{(e)}$, the shear component. They are calculated with the following equations:

$$K_{mm}^{(e)} = \sum_{k=1}^{N} \int_A B_m^T A B_m (z_{k+1} - z_k) dA \tag{2.32}$$

$$K_{mb}^{(e)} = \sum_{k=1}^{N} \int_A B_m^T B B_b \frac{1}{2} (z_{k+1}^2 - z_k^2) dA \tag{2.33}$$

$$K_{bm}^{(e)} = \sum_{k=1}^{N} \int_A B_b^T B B_m \frac{1}{2} (z_{k+1}^2 - z_k^2) dA \tag{2.34}$$

$$K_{bb}^{(e)} = \sum_{k=1}^{N} \int_A B_b^T D B_b \frac{1}{3} (z_{k+1}^3 - z_k^3) dA \tag{2.35}$$

$$K_{ss}^{(e)} = \sum_{k=1}^{N} \int_A B_s^T S B_s (z_{k+1} - z_k) dA \tag{2.36}$$

where

$$[A] = \begin{bmatrix} A_{11} & A_{12} & A_{13} \\ A_{12} & A_{22} & A_{23} \\ A_{13} & A_{23} & A_{66} \end{bmatrix} \tag{2.37}$$

$$[S] = \begin{bmatrix} A_{44} & A_{45} \\ A_{45} & A_{55} \end{bmatrix} \tag{2.38}$$

$$[B_m]^{(e)} = \begin{bmatrix} \frac{\partial N_j}{\partial x} & 0 & 0 & 0 & 0 \\ 0 & \frac{\partial N_j}{\partial y} & 0 & 0 & 0 \\ \frac{\partial N_j}{\partial y} & \frac{\partial N_j}{\partial x} & 0 & 0 & 0 \end{bmatrix} \tag{2.39}$$

$$[B_b]^{(e)} = \begin{bmatrix} 0 & 0 & 0 & \frac{\partial N_j}{\partial x} & 0 \\ 0 & 0 & 0 & 0 & \frac{\partial N_j}{\partial y} \\ 0 & 0 & 0 & \frac{\partial N_j}{\partial y} & \frac{\partial N_j}{\partial x} \end{bmatrix} \tag{2.40}$$

$$[B_s]^{(e)} = \begin{bmatrix} 0 & 0 & \frac{\partial N_j}{\partial x} & N_j & 0 \\ 0 & 0 & \frac{\partial N_j}{\partial y} & 0 & N_j \end{bmatrix} \tag{2.41}$$

and

$$j = 1 \ldots 4. \tag{2.42}$$

The shape function derivatives used in the previous equations are calculated as follows:

$$\begin{bmatrix} \frac{\partial N_j}{\partial x} \\ \frac{\partial N_j}{\partial y} \end{bmatrix} = [J]^{-1} \begin{bmatrix} \frac{\partial N_j}{\partial \xi} \\ \frac{\partial N_j}{\partial \eta} \end{bmatrix}, \tag{2.43}$$

and the Jacobian, J, is

$$[J] = \begin{bmatrix} \frac{\partial x}{\partial \xi} & \frac{\partial y}{\partial \xi} \\ \frac{\partial x}{\partial \eta} & \frac{\partial y}{\partial \eta} \end{bmatrix} \tag{2.44}$$

where the partial derivatives of x and y are calculated with the following equation

$$\frac{\partial x}{\partial \xi} = \sum_{j=1}^{4} \frac{\partial N_j}{\partial \xi} X_j \tag{2.45}$$

$$\frac{\partial y}{\partial \xi} = \sum_{j=1}^{4} \frac{\partial N_j}{\partial \xi} Y_j \tag{2.46}$$

X_j and Y_j are the coordinates of node j and the equations for the shape functions are

$$N_1 = \frac{1}{4}[(1-\xi)(1-\eta)] \tag{2.47}$$

$$N_2 = \frac{1}{4}[(1+\xi)(1-\eta)] \tag{2.48}$$

$$N_3 = \frac{1}{4}[(1+\xi)(1+\eta)] \tag{2.49}$$

$$N_4 = \frac{1}{4}[(1-\xi)(1+\eta)] \tag{2.50}$$

where ξ and η are the values from the Gaussian quadrature numerical integration method.

The mass matrix is calculated using the *consistent* mass matrix formulation. Equation (2.51) is the equation for the elemental mass matrix and the global mass matrix is assembled in the same manner as the global stiffness matrix

$$M^e = \int \rho N^T N dV. \tag{2.51}$$

With the calculations of the global mass and stiffness matrices complete, the general eigenproblem, Equation (2.3), can be solved. Many numerical methods for solving this problem exist, but the number of solution options available will vary based on the linear algebra library used. The method used in this thesis is symmetric bidiagonalization followed by QR reduction. This will be expanded upon further in Chapter 3.

2.2 Optimization of Orthotropic Material Orientation

Optimization is a mathematical process in which an objective function is minimized or maximized while satisfying any imposed constraints. The optimization problem encountered in this thesis is the maximization of eigenfrequencies and eigenfrequency band gaps

in plates constructed from orthotropic material (unidirectional pre-preg carbon fiber). The optimization problem can be formulated as:

$$\text{maximize} : \omega_i(\theta_n), \tag{2.52}$$

$$\text{subject to} : (K - \omega_i^2 M)\phi_i = 0 \tag{2.53}$$

There are numerous optimiaztion methods, ranging from evolutionary optimization to gradient-based methods, each with their own strengths and weaknesses. The optimization problem encountered in this thesis requires a large number of design variables, and therefore only gradient based methods were considered. Of the gradient-based methods, the steepest descent method was selected for use.

2.2.1 Steepest Descent Method

The steepest descent method was selected for its simplicity and ease of implementation. As described in its name, this method calculates the steepest descent direction and then calculates the size of step to take in that direction. To determine the maximum, instead of the minimum, a small modification had to be made to this algorithm. Specifically, calculating the steepest *ascent* instead of steepest *descent*. The major steps of this algorithm are as follows:

1. Set starting point for design variables: θ_n^0, $n = 1, 2, \ldots N$,
2. Solve for objective function, $f(\theta_n)$,
3. Calculate gradient, $g(\theta) = \nabla f(\theta_n)$, and then ascent direction, $p_i = g(\theta_n)/||g(\theta_n)||$,
4. Calculate step size α_i in direction of p_i using line search method,
5. Update design variables, $\theta_n^{i+1} = \theta_n^i + \alpha_i p_i$,

6. Solve for new objective function. Stop if convergence criteria are satisfied, otherwise $i = i + 1$ and return to step 3.

where θ_n is the vector of fiber angles, N is the number of elements, and i is the current iteration number. The sensitivity analysis, step size calculations, and convergence criteria can vary depending on the user's requirements. The sensitivity analysis and line search methods used in this thesis will be expanded upon in the upcoming subsections. The convergence criteria used determines convergence based on the magnitude of successive changes in the objective function falling under a user defined limit. The equation is:

$$|f(\theta_n^{i+1} - \theta_n^i)| \leq \epsilon_a + \epsilon_r |f(\theta_n^i)|, \tag{2.54}$$

where ϵ_a is the absolute tolerance, which is set to $\epsilon_a = 10^{-6}$, and ϵ_r is the relative tolerance, which is set at $\epsilon_r = 0.001$. If this convergence criterion is satisfied for three successive iterations, the optimization process has converged and the program will break out of the iterative optimization loop.

2.2.2 Sensitivity Analysis

Gradient-based optimization methods depend on the sensitivity analysis to calculate the gradients that are integral to the optimization process. The gradients are the derivatives of the objective function(s) with respect to the design variables, and they are calculated using the finite difference method in this thesis. It is not a very efficient method and it is only a first order approximation, but it is simple to implement and easy to parallelize. The equation is:

$$\frac{\mathrm{d}f}{\mathrm{d}x_i} = \frac{f(x_i + h) - f(x_i)}{h}, \tag{2.55}$$

where h is the finite difference interval. Its concurrency results from its ability to calculate the derivative with respect to a design variable independently from all other derivative

calculations. The results of parallelization will be presented in Section 3.1.1.

2.2.3 Function Maximization

The golden section search method is used to calculate the maximium step size, α_k, for the optimization program to take in the steepest ascent direction. This method begins by bracketing a search interval, $[a, b]$, then two initial points, α_1 and α_2, are calculated using the golden ratio, $\varphi = (1 + \sqrt{5})/2 \simeq 0.618$. The starting α values are calculated as follows:

$$\alpha_1 = a + (b - a)(1 - \varphi)$$

$$\alpha_2 = a + (b - a)\varphi$$

The iterative proces starts by evaluating the objective function, $f(\theta_n^k + \alpha_k p_k) = f(\alpha)$, for the initial α values, then proceeds to reduce the search interval for the optimal value of α using the golden ratio φ. This continues until the size of the search interval satisfies the convergence criterion, ϵ, which is a limit on the minimum size. The algorithm is as follows:

For the optimziation performed in this thesis, the convergence criterion is typically set to $\epsilon = 0.1$. With the golden search complete the design variables are updated and the optimization process starts its next iteration.

while $|f(\alpha_1) - f(\alpha_2)| \geq \epsilon$ **do**
  if $(f(\alpha_1) \geq f(\alpha_2)$ **then**
    $a = \alpha 1$
    $\alpha_1 = \alpha_2$
    $f(\alpha_1) = f(\alpha_2)$
    $\alpha_2 = a + (b - a)\varphi$
    Recalculate $f(\alpha_2)$
  else
    $b = \alpha_2$
    $\alpha_2 = \alpha_1$
    $f(\alpha_2) = f(\alpha_1)$
    $\alpha_1 = a + (b - a)(1 - \varphi)$
    Recalculate $f(\alpha_1)$
  end if
end while

2.3 Modal Analysis

In order to validate the optimization calculations, plates will be fabricated from unidirectional prepreg carbon fiber tape and subjected to modal testing to determine their natural frequencies. Modal analysis is a process in which the dynamic properties, such as natural frequencies and damping, of a structure are determined by exciting the structure and measuring its response. Various methods are available for both excitation and measurement.

Two popular excitation methods are the shaker and impact hammer. For small objects, such as the plates that will be tested for this thesis, a shaker would attach to the structure through an armature called a stinger which transmits the force from the shaker to the structure. The excitation produced by a shaker is controlled by an input signal which is set by the user. Common modal testing signals include a swept sine and random frequency vibration profiles. A force transducer embedded in the shaker is used to measure the force input. The impact hammer is used to provide an impulse to the structure which excites a range of vibration modes, with the contact time of the hammer tip inversely proportional to the size of the range of frequencies excited. An ideal impact would have an infinitely

small contact time which would provide the perfect impulse and excite all modes of vibration with equal energy. The impact force is measure by a transducer located in the hammer tip. The modal testing performed for in this thesis will use an impact hammer.

Two methods exist for measuring the response of the structure. One is the use of a laser vibrometer which can measure the response at a single point or multiple points simultaneously, depending on the device. The more common method of response measurement is to use an accelerometer, which is what will be used in this thesis. Both the force transducer and accelerometer provide an analog voltage signal which is sent to the data aquisition system for signal conditioning and analog to digital conversion (ADC). The ADC converts the continuous-time signal to a discrete-time signal and this is the data that can be viewed and analyzed. When sampling the response signal it is neccessary to remember that the highest measured frequency is one half of the sample frequency, as shown in Equation (2.56). This is known as the Nyquist frequency. Figure 2.4 shows an example of the discrete time signal recorded from the impact and response on a cantilevered aluminum flat bar.

$$F_N = \frac{F_s}{2}, \tag{2.56}$$

where F_N is the Nyquist frequency and F_s is the sampling frequency.

To determine the natural frequencies of the tested structure, the discrete-time data needs to be analyzed in the frequency domain. To convert the data to the frequency domain, the fast Fourier transform (FFT) algorithm is used to calculate the discrete Fourier transform (DFT). The frequency response of the structure can be determined by calculating the frequency response function (FRF), $H(f)$, as shown in Equation 2.57 [8].

$$H(f) = \frac{S_{xy}}{S_{xx}}, \tag{2.57}$$

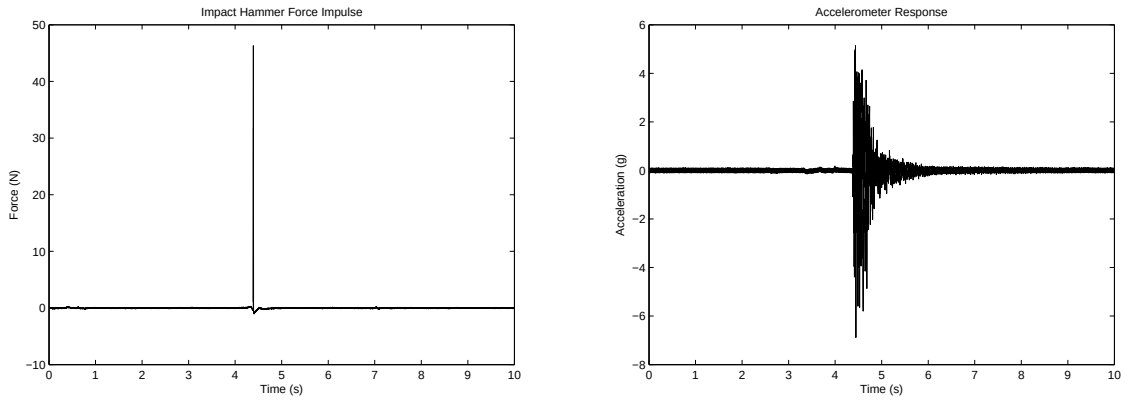

(a) Impact hammer impulse (b) Response of aluminum bar

Figure 2.4: Impact hammer impulse and response discrete-time signal from aluminum flat bar

where S_{xx} is the power spectrum of the excitation signal and S_{xy} is the cross power spectrum. The equations for the power spectra are:

$$S_{xx} = \frac{FFT(x) \times FFT^*(x)}{N^2}, \tag{2.58}$$

$$S_{xy} = \frac{FFT(y) \times FFT^*(x)}{N^2}, \tag{2.59}$$

where the asterisk after FFT denotes that the conjugate is used, x and y are the excitation and response data, respectively, and N is the number of samples in the data set. The frequency response function derived from the data presented in Figure 2.4 is shown in Figure 2.5. Using commercial FEA software, the first four natural frequencies of the bar were calculated to be: 27.1, 169.8, 171.3, and 474.8 Hz, which approximately matches up with the peaks in the FRF. To obtain a better estimate of the natural frequencies calculated in the FRF it is possible to apply a modal parameter extraction technique, but its accuracy may be limited by the amount of noise present in the signal.

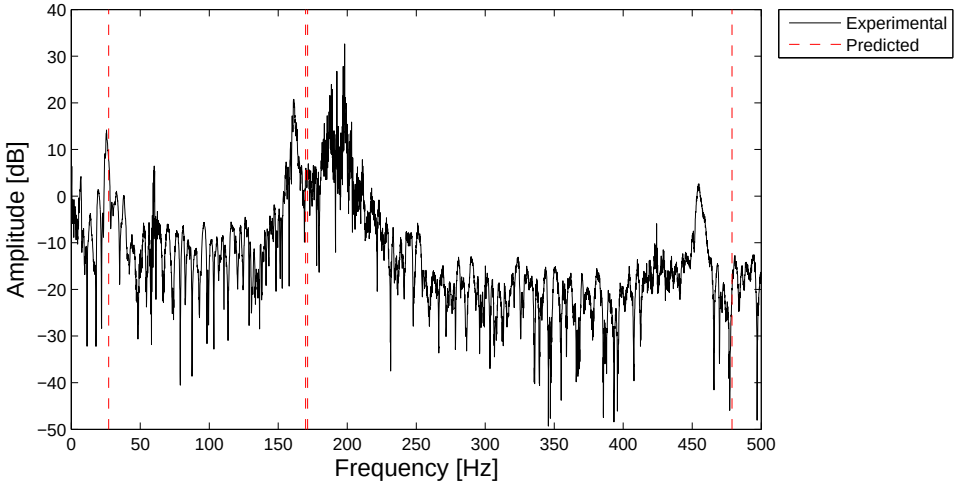

Figure 2.5: FRF of cantilevered aluminum flat bar

Chapter 3

Optimization

3.1 Implementation

The optimization program was written in C/C++ and uses the GNU Scientific Library (GSL) for handling of the matrices, vectors, and linear algebra [1]. It optimizes the fiber orientations throughout a rectangular plate for the maximization of specified eigenfrequencies or eigenfrequency band gaps. The plate dimensions, ply thickness, ply configuration (which plies are optimized and which ones remain unidirectional), material properties, number of elements to use, boundary conditions, and objective function are all user specified. Ply thickness is constant for all plies.

The problem is first initialized by defining the dimensions of the plate, `xDim` and `yDim`, and the number of elements to use `nelx` and `nely`. These values are used as inputs into the `quadmesh()` function which calculates the node coordinates and constructs elements from these nodes, both of which are stored in a GSL matrix structure, `nodeCoordinates` and `elementNodes`, respectively. With the discretization complete only the material properties and ply configuration need to be set before the finite element calculations can begin. Both the stiffness and mass matrices, K and M, are GSL matrices and they are constructed with the `CLT_stiffness_matrix()` and `CLT_mass_matrix()` functions,

respectively.

The boundary conditions are set by the `BC_type` variable. This variable is a `string` and it is used as an input into the function `CLT_bc()` which calculates the fixed nodes and their degrees of freedom for a rectangular plate. The fixed degrees of freedom are then eliminated from the stiffness and mass matrices before calculating the objective function. Four steps are required to solve the general eigenproblem using GSL functions and they are all contained within the function called `eigensolve()` which returns the objective function as a `double`. First, a vector, matrix, and workspace are initialized. The vector and matrix, `eval` and `evec` respectively, are used to store the final eigenvalues and eigenvectors, and the workspace, `w`, is used in the calculations. To solve for the eigenvalues and eigenvectors, the function `gsl_eigen_gensymmv()` is called to solve the real general symmetric-definite eigensystem, as defined in Equation (2.1), and it has the stiffness and mass matrices along with `eval`, `evec`, and `w` as arguments. A GSL sorting function, `gsl_eigen_gensymmv_sort()`, is then used to sort the eigenvalues and eigenvectors. The eigenfreqeuncies are calculated by finding the root of the eigenvalues as shown in Equation(2.2), and the units of the frequencies are radians per second. Lastly, the relevant value, specified by the `eigNumber` variable which is an input argument, is returned.

Two functions comprise the majority of computational load in the optimization portion of the program. These are the gradient function, `CLT_grad()`, which calculates the sensitivities of each element, and the golden search function, `CLT_golden()`, which calculates the optimal step size using the golden section method. The optimization calculations are contained within a `while` loop which is set to break if the convergence criteria are met. As discussed earlier in Chapter 2, the gradients (sensivities) are calculated using the finite difference method, which is shown in Equation (2.55). These gradients are used to find the ascent direction, which is the direction the design variables have to travel to increase

the objective function. The golden section search function, `CLT_golden()`, calculates the size of step to take in the ascent direction. The new objective function is then compared to the old one and is judged on whether it is coverging to a solution. If the objective function has converged, the program breaks out of the optimization calculations and writes the final fiber angles into a csv file which can then be plotted in Matlab.

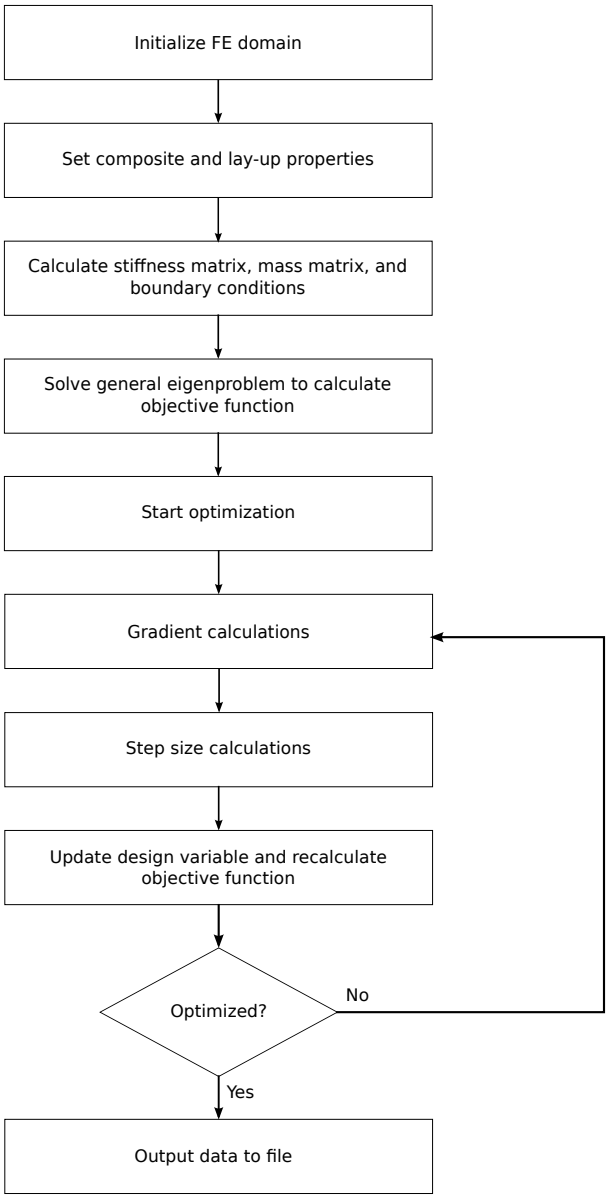

Figure 3.1: Flowchart of optimization program

3.1.1 Parallelization

Since the sensitivity of each element can be calculated independently from the rest, the gradient calculations are a prime candidate for parallelization. Additionally, the gradient calculations comprise of approximately 80% of the computational load when the optimization program is run in serial, according to the profiling done in Matlab shown in Figure 3.1.1, and therefore the addition of parallelized gradient calculations should provide a signifcant decrease in computational time. This will also allow for optimizing plates with a higher resolution mesh within reasonable time constraints. To make the most of the concurrency of the gradient calculations, the optimization program was run on the General Purpose Cluster (GPC) on SciNet.

Parents (calling functions)
No parent

Lines where the most time was spent

Line Number	Code	Calls	Total Time	% Time	Time Plot
83	grad = eig_gradient2(eig_numbe...	13	754.019 s	80.4%	
97	[alpha_test,f_obj_test,theta_t...	13	172.264 s	18.4%	
105	[Vnew,Dnew] = eig(stiffness_ne...	13	6.294 s	0.7%	
103	domainPlot(numberElements,thet...	13	2.803 s	0.3%	
104	[stiffness_new] = formStiffnes...	13	0.811 s	0.1%	
All other lines			1.185 s	0.1%	
Totals			937.376 s	100%	

Children (called functions)

Function Name	Function Type	Calls	Total Time	% Time	Time Plot
eig_gradient2	M-function	13	754.016 s	80.4%	
golden_eig2	M-function	13	172.264 s	18.4%	
domainPlot	M-function	15	3.129 s	0.3%	
formStiffnessMatrixMindlinQ4composite3	M-function	14	0.882 s	0.1%	
formMassMatrixMindlinQ4	M-function	1	0.054 s	0.0%	
EssentialBC	M-function	1	0.014 s	0.0%	

Figure 3.2: Profile of Matlab optimization code

The parallelized gradient calculations were performed using a hybrid OpenMP/MPI approach. Open MPI is an open source message passing interface (MPI) library which was used to communicate between nodes on the GPC [2]. OpenMP is an API for shared

memory parallel processing and it was used for perfroming parallel calculations across the processors of each node [3]. An example of the parallelization process using 3 nodes is shown in Figure 3.1.1.

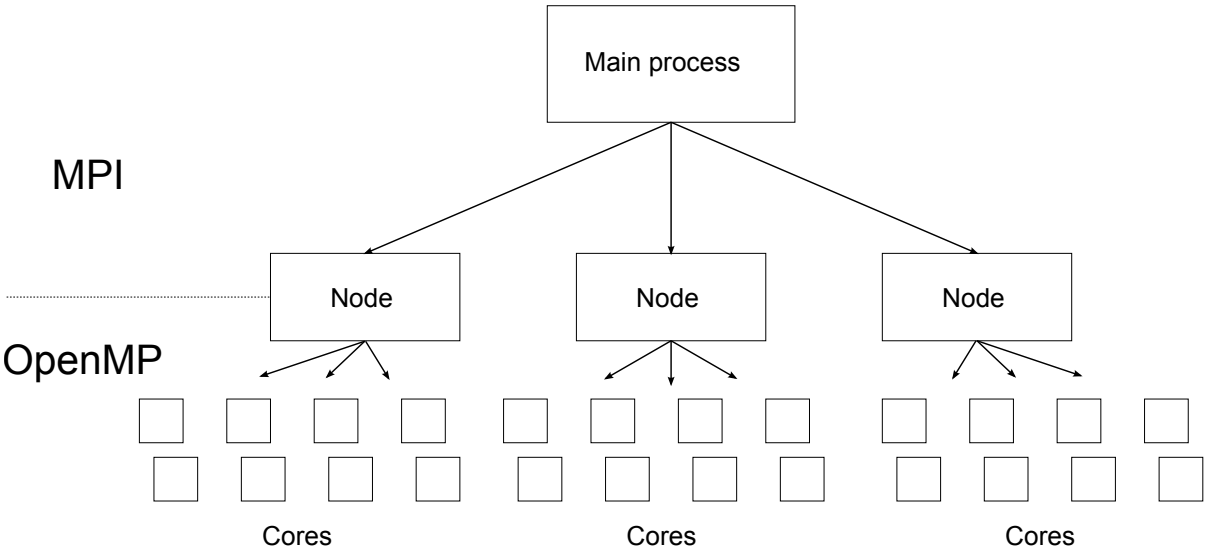

Figure 3.3: Organization of parallel calculations

To demonstrate the performance gained from the use of parallel programming the optimization program was run with varying numbers of nodes (each node containing 8 processors). Data was collected for two different meshes of the plate, 18x6 and 24x8 elements, and plotted in Figure 3.4. From these plots it can be seen that the use of parallel processing greatly reduces the computational time required by the optimization program.

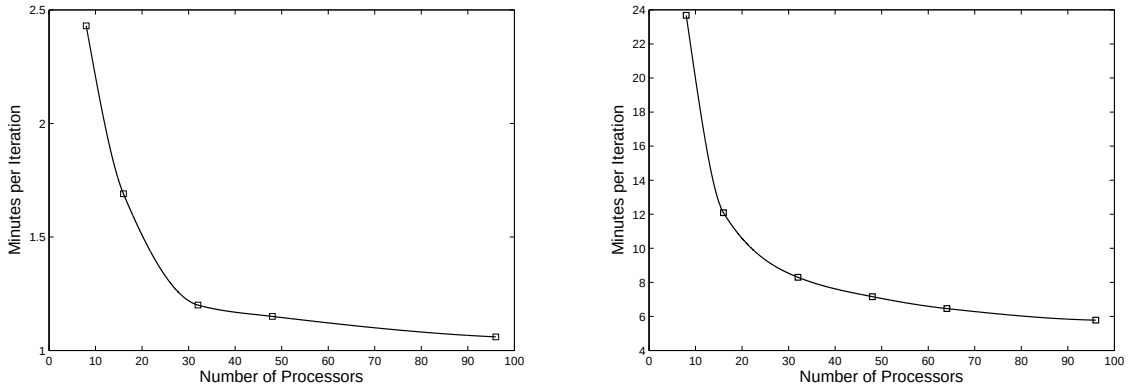

(a) 18x6 element mesh

(b) 24x8 element mesh

Figure 3.4: The effect of parallelization on computation time for various mesh sizes

3.2 Results

Plates of the size 9" by 3" were optimized with varying mesh sizes, ranging from 18x6 up to 30x10, as shown in Figure 3.2. The objective functions maximized the 1st to 6th eigenfrequencies and also all eigenfrequency band-gaps within that range. The orthotropic material used in the simulations is an approximation of the unidirectional prepreg carbon fiber which will be used to fabricate the test samples. These material properties were also used when verifiying the optimization results with the commercial FEA software package ABAQUS. The results from the ABAQUS calculations will be presented with the optimization results. The material properties are listed below.

$$E_1 = 107 \text{ GPa}$$

$$E_2 = 10 \text{ GPa}$$

$$v_{12} = 0.27$$

$$G_{12} = 4 \text{ GPa}$$

$$G_{13} = 4 \text{ GPa}$$

$$G_{23} = 1.728 \text{ GPa}$$

$$\rho = 1384 \text{ kg/m}^3$$

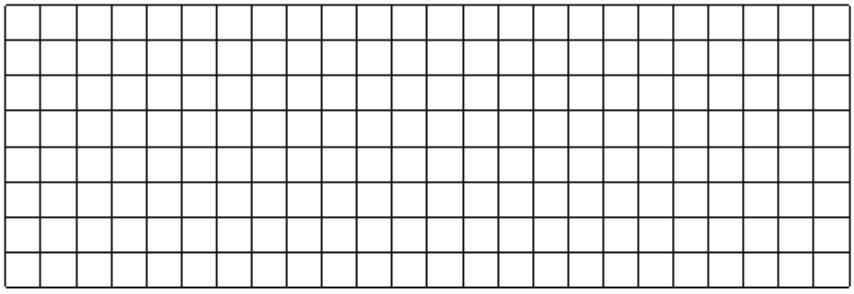

Figure 3.5: 24x8 element mesh on a 9x3 inch plate

The Young's modulus and Poisson's ratio were obtained from tensile tests conducted on unidirectional samples. The results from the test are shown in Figure 3.2. The other properties are from material specification sheets. For tensile testing the unidirectional specimen was loaded parallel to its fibers and had two strain gauges attached; one parallel to the fibers and one perpendicular. A laser extensometer was also used to for a secondary measurement of strain. The force measurements were recorded by the Material Testing System (MTS) load frame.

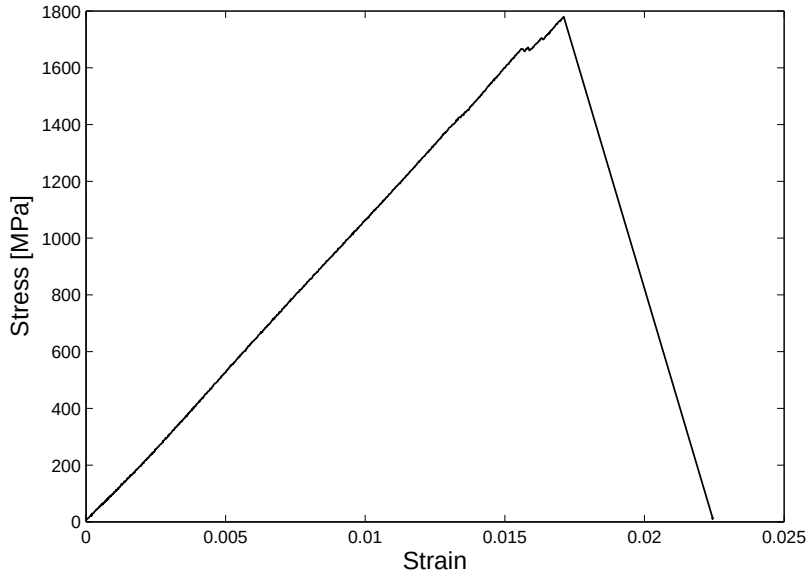

Figure 3.6: Unidirectional prepreg carbon fiber tensile test results

Young's modulus is

$$E = \frac{\sigma}{\epsilon}, \tag{3.1}$$

where the strain, ϵ, is measured by the longitudinal strain gauge, and the nominal stress, σ, is calculated with

$$\sigma = \frac{F}{A}, \tag{3.2}$$

and A is determined from the initial dimensions of the test specimen. The equation for Poisson's ratio is

$$\nu_{12} = \frac{\epsilon_{transverse}}{\epsilon_{longitudinal}}, \tag{3.3}$$

where both of the strains are measured with the strain gauges.

3.2.1 Single Eigenfrequencies

Fiber angles were first optimized for the maximization of single eigenfrequencies to test the optimization algorithm. Additionally, the results from single eigenfrequency optimization are more intuitive than the band gap results and therefore it is easier to anticipate the correct final solution. For both the single eigenfrequency and band gap optimization a cantilevered boundary condition is used (left side is fixed) and the optimization starts from every fiber angle set to zero, unless stated otherwise. The results are presented in the form of a figure of the optimized fiber orientations and a plot of the convergence of the objective function. The ABAQUS verification calculations are also presented with their respective optimization results. The results for the higher frequencies may also include additional figures for results from higher resolution meshes which were required to solve accurately for the more complex mode shapes.

The first three odd number eigenfrequencies are predominantly bending modes, and therefore the optimal fiber orientations for maximizing these eigenfrequencies will be mostly unidirectional, perpendicular to the cantilevered boundary condition. The mode shapes can be seen in Figure 3.7. Since the optimal ply for these three modes is unidirectional at 0°, the initial condition of the plies designated to be optimized was changed to 45°. Figure 3.8 shows the optimized fiber angles and it can be seen that some fibers did not end up at 0°; they remained at 45° or somewhere between due to the insensitivity of of the vibrational response to these fiber angles. Figures 3.9-3.11 show the convergence of the optimization calculations.

The optimal fiber angles for maximizing these three bending modes all experience some correlation with each other. The third and fifth modes are strongly correlated to the first mode due to all three modes being heavily dependent on the fiber angles close to the cantilevered boundary condition. This can be observed when the fiber angles

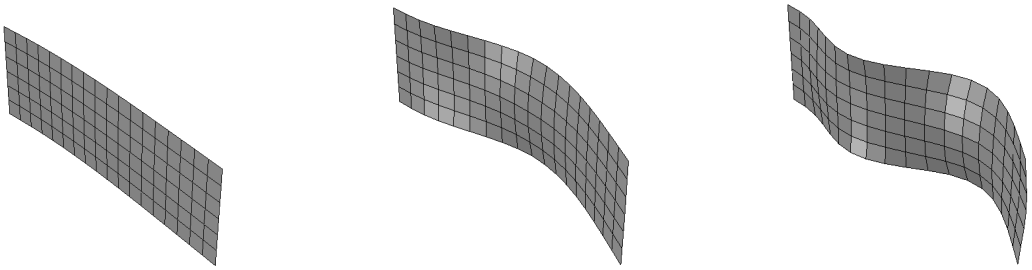

(a) 1^{st} mode (b) 3^{rd} mode (c) 5^{th} mode

Figure 3.7: Mode shapes for bending eigenfrequencies

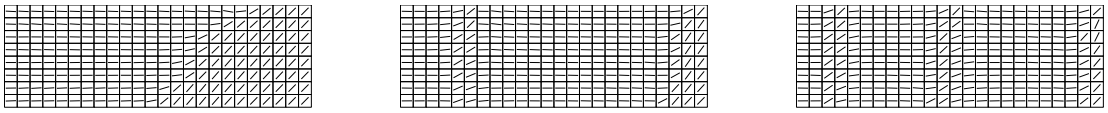

(a) 1^{st} mode (b) 3^{rd} mode (c) 5^{th} mode

Figure 3.8: Optimized fiber angles for maximizing the frequencies associated with the first three bending modes

are optimized to maximize the $1-3$ and $1-5$ gaps. The optimal fiber layout remains mainly unidirectional and a negligible increase in the bandgap size is produced. On the other hand, the third and fifth modes are only slightly correlated to each other, as observed when maximizing the $3-5$ gap where an increase in approximately 30 Hz is produced. Section 3.2.3 will provide more details on these arbitrary eigenfrequency gap maximization results.

The second mode of vibration is the first torsional mode and its optimization follows the typical convergence profile observed and converges after 19 iterations, as shown in Figure 3.13. Starting from the second eigenfrequency of the unidirectional plate, which is approximately 50 Hz, the optimization process converges to a solution with a second

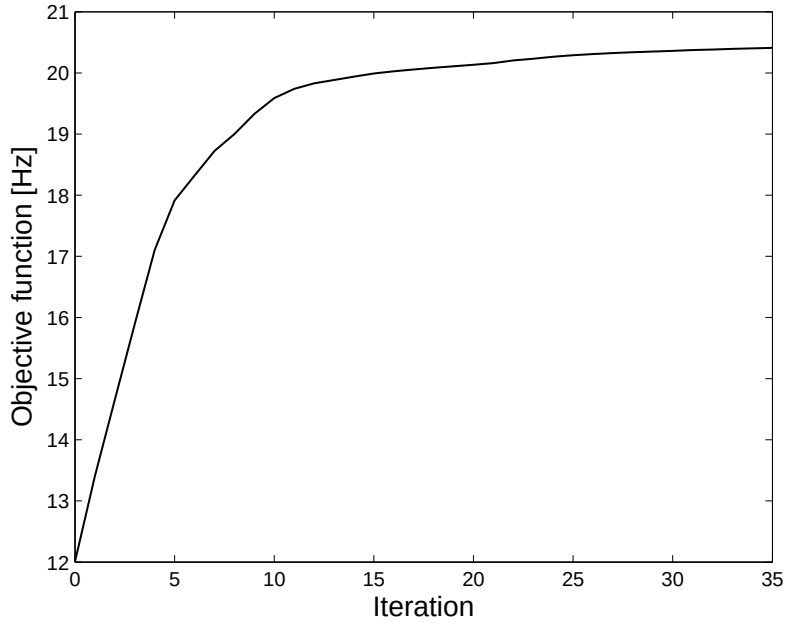

Figure 3.9: Convergence for the maximization of the 1st eigenfrequency from 45° start

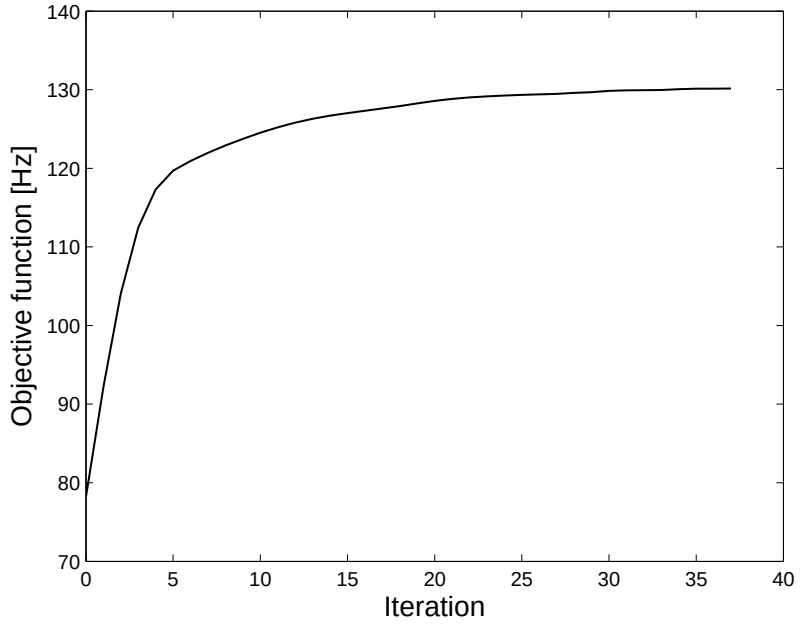

Figure 3.10: Convergence for the maximization of the 3rd eigenfrequency from 45° start

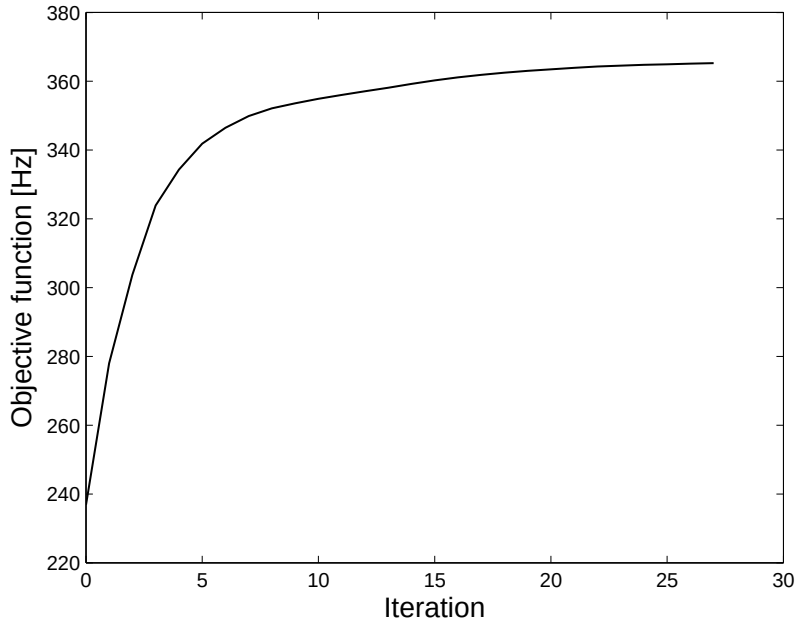

Figure 3.11: Convergence for the maximization of the 5^{th} eigenfrequency from 45° start

eigenfrequency of approximately 85 Hz. The optimized fiber angles are shown in Figure 3.12 along with its mode shape.

The optimization for the maximization of the fourth eigenfrequency follows the same typical convergence profile as seen previously. The fourth eigenfrequency begins at approximately 185 Hz and converges to a final eigenfrequency of approximately 272 Hz after 18 iterations. The fiber angles of the optimized ply are shown in Figure 3.14 along with the relevant mode shape. The convergence of the optimization process is shown in Figure 3.15.

The optimization for the maximization of the sixth eigenfrequency starts from approximately 384 Hz and increases to approximately 486 Hz after 15 iterations. The final fiber angles along with the mode shape of the sixth eigenfrequency are shown in Figure 3.16 and the convergence is plotted in Figure 3.17.

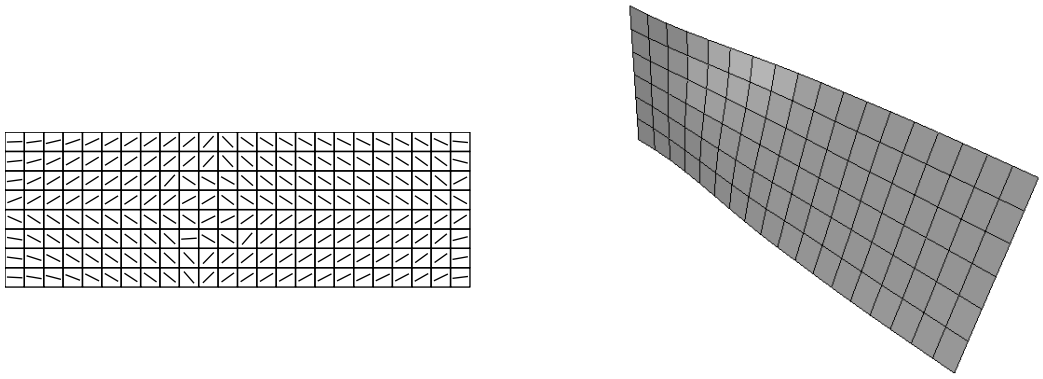

(a) Optimized fiber angles (b) Mode shape

Figure 3.12: Comparison of optimized fiber angles to mode shape for the 2nd eigenfrequency

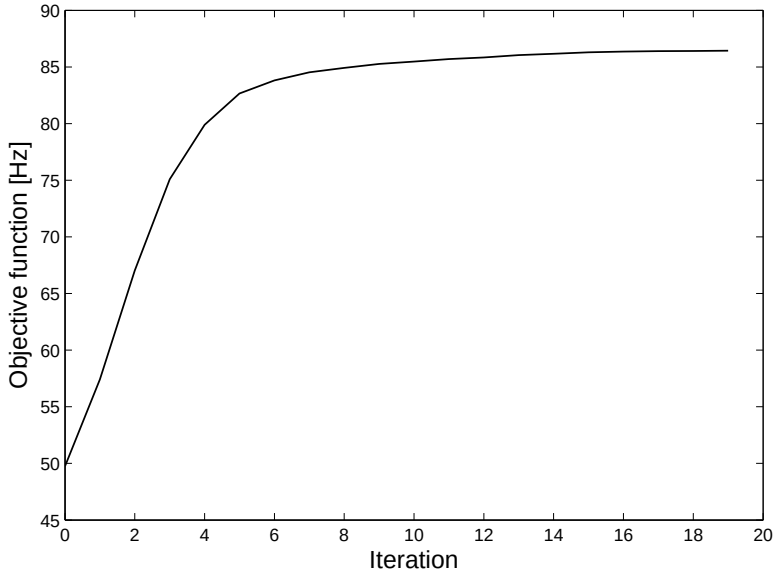

Figure 3.13: Convergence for the maximization of the 2nd eigenfrequency

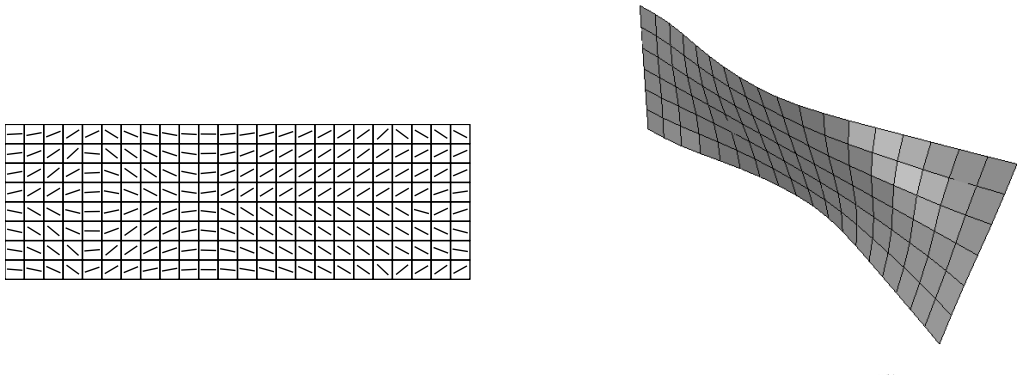

(a) Optimized fiber angles (b) Mode shape

Figure 3.14: Comparison of optimized fiber angles to mode shape for the 4^{th} eigenfrequency

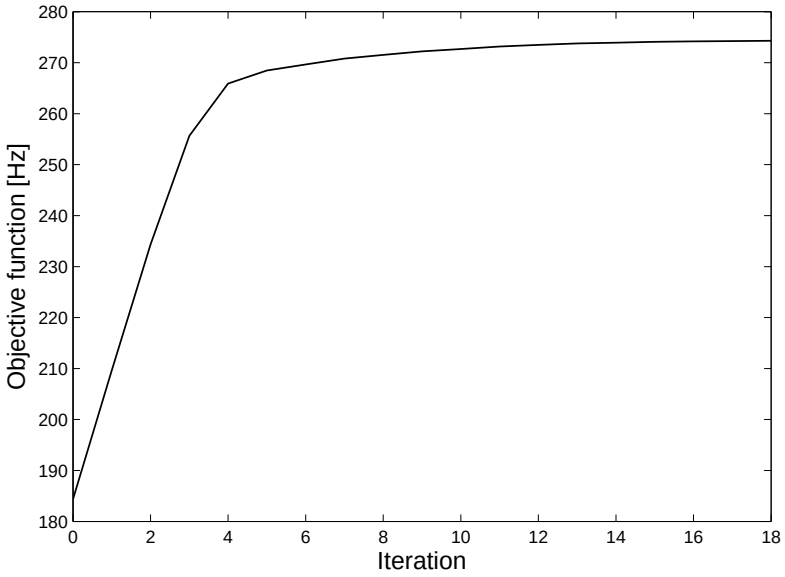

Figure 3.15: Convergence for the maximization of the 4^{th} eigenfrequency

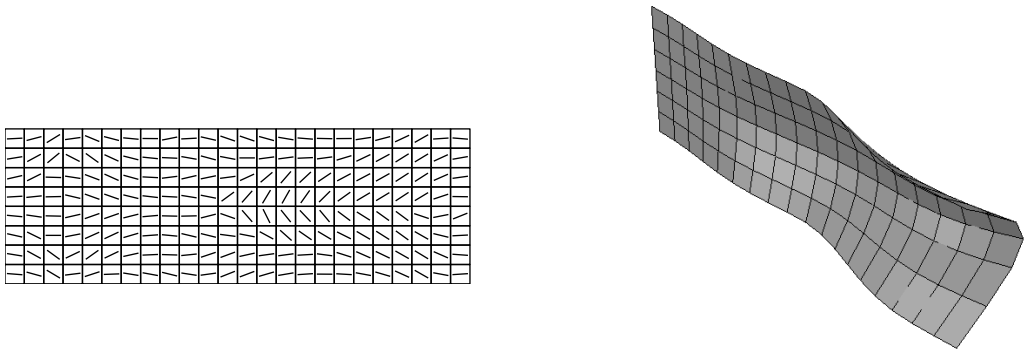

(a) Optimized fiber angles (b) Mode shape

Figure 3.16: Comparison of optimized fiber angles to mode shape for the 6^{th} eigenfrequency

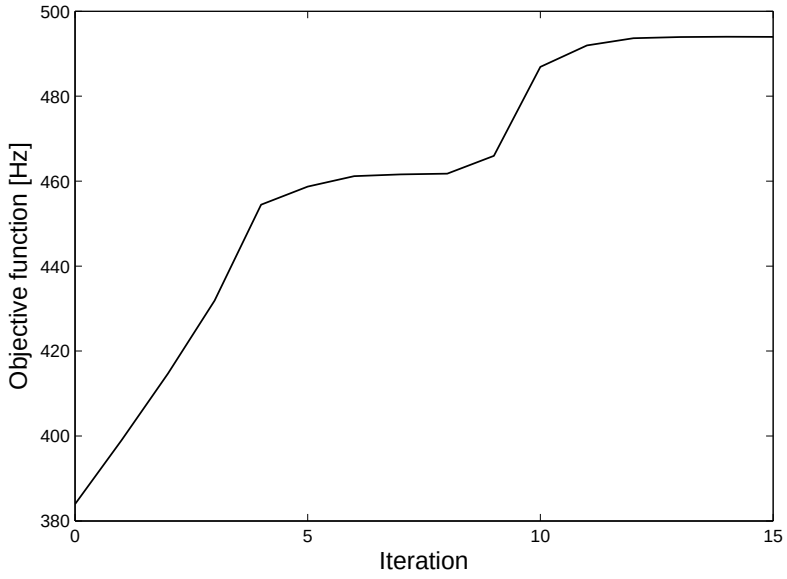

Figure 3.17: Convergence for the maximization of the 6^{th} eigenfrequency

As the mode number increases the complexity of the mode shapes increases. At a certain point the resulting optimized fiber angles become too complex to lay-up by hand and the eigenfrequecy becomes too difficult to measure with modal testing. With an increase in mode shape complexity the optimization process will have to use a higher resolution mesh as well, which will greatly increase the computational time required. Therefore the optimization process was only used up to the sixth mode of vibration.

3.2.2 Eigenfrequency Bandgaps

This section presents the results of the band gap optimization calculations, which is the main objective of this thesis. The results are presented in the format used in the previous section with the addition of comparisons to related single eigenfrequency optimization results. Beginning with the first band gap, which is the distance between the first and second eigenfrequencies, the optimized fiber angles are shown in Figure 3.18 and they are almost identical to the optimized fiber angles for the maximization of the second eigenfrequency. The bandgap begins the optimization at approximately 29 Hz (unidirectional plate) and increases to approximately 72 Hz after 20 iterations, as shown in Figure 3.19.

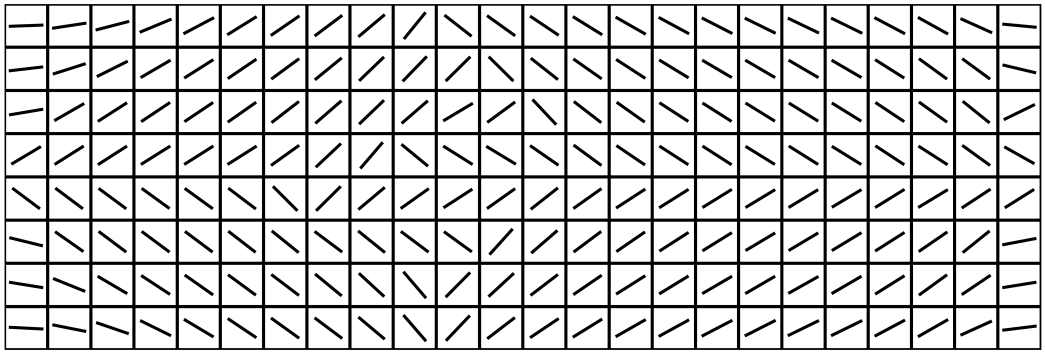

Figure 3.18: Results of optimization for maximization of the bandgap between the 1st and 2nd eigenfrequencies

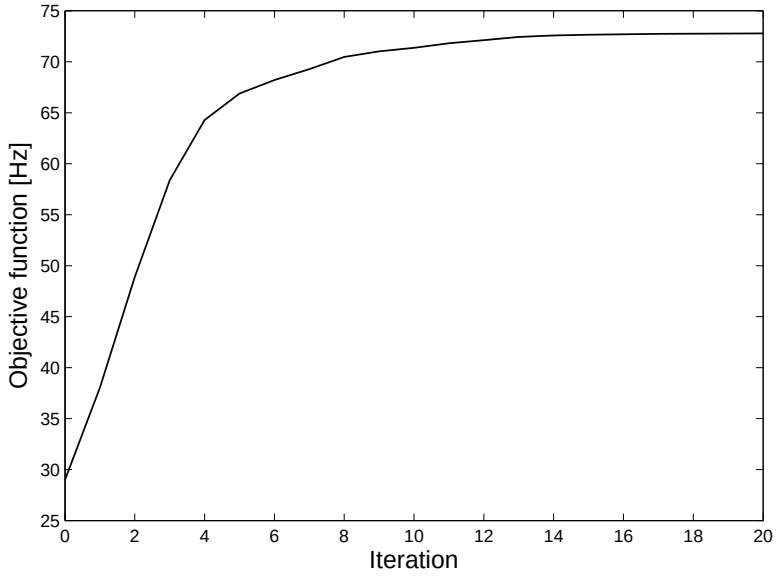

Figure 3.19: Convergence for the maximization of the bandgap between the 1st and 2nd eigenfrequencies

	Modes					
Description	1	2	3	4	5	6
Optimized	13.66	85.71	90.16	290.85	262.38	428.71
ABAQUS	14.20	85.23	91.90	240.39	269.12	429.19

Table 3.1: Eigenfrequencies calculated from optimized results from maximization of the 1st and 2nd eigenfrequencies

Table 3.1 presents the eigenfrequencies calculated with both the opimized results and the ABAQUS approximation of the results. The differences between the values calculated for each mode are minimal except for the fourth mode where there is an approxiately 50 Hz difference. The cause of this large discrepancy could be attributed to the approximations made to the optimized results to aid in modeling the layup in ABAQUS. During the modeling the fibre angles were rounded to the nearest multiple of 5 and some fiber angles were also adjusted for symmetry. These adjustments would have the largest

impact on the center of the plate where the fibers switch direction. This area has some fibers with angles that don't seem to follow the pattern observed in the rest of the plate; coincidentally, this area is also near an inflection point in the fourth mode shape, so a change to the fiber angles in this area could affect the performance of the plate with respect to the fourth mode.

When optimizing for the maximization of the bandgap between the second and third eigenfrequencies it was found that the optimized fiber angles do not differ much from the unidirectional starting condition, as can be seen in Figure 3.20. With minimal change in the fiber angles there will be minimal change in the vibrational characteristics of the composite plate, which can be seen in the convergence plot Figure 3.21. The optimization procedure required only 8 iterations and the bandgap only increased by approximately 2 Hz. In Table 3.2 the eigenfrequencies of the optimized plate are compared to the results of calculations performed in ABAQUS on a 5 ply unidirectional plate (optimized lay-up is assumed to be unidirectional). The eigenfrequencies from the two sources are very similar and only diverge slightly as the mode number increases.

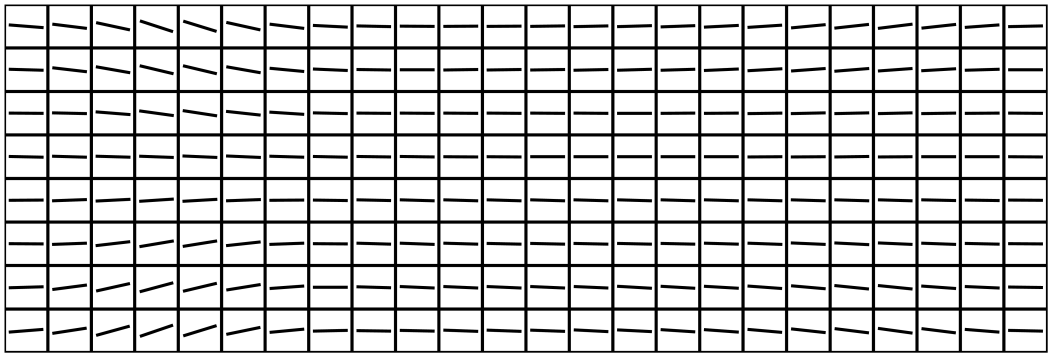

Figure 3.20: Results of optimization for maximization of the bandgap between the 2nd and 3rd eigenfrequencies

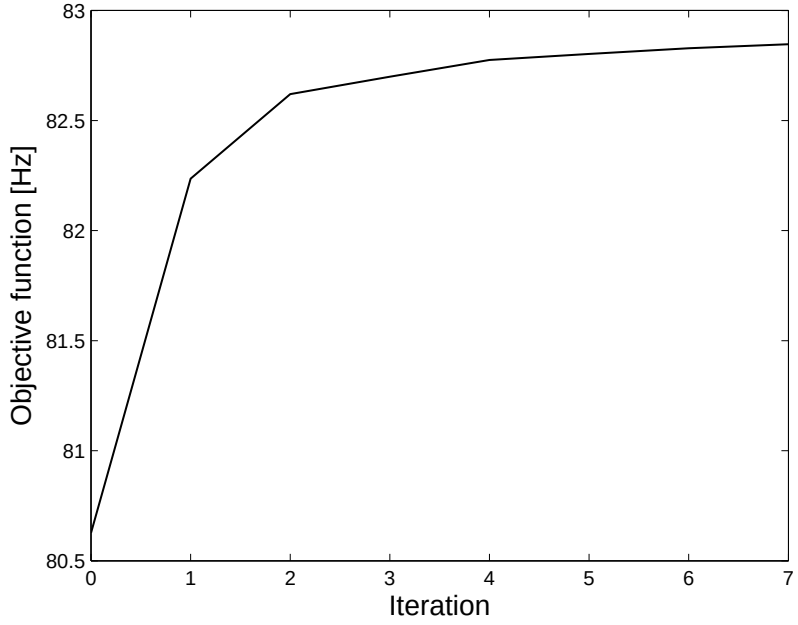

Figure 3.21: Convergence for the maximization of the bandgap between the 2nd and 3rd eigenfrequencies

	Modes					
Description	1	2	3	4	5	6
Optimized	20.30	46.75	129.60	187.34	359.35	387.25
ABAQUS	20.72	49.72	129.98	183.73	363.35	379.47

Table 3.2: Eigenfrequencies calculated from optimized results from maximization of the 2nd and 3rd eigenfrequencies

The optimized fiber angles for the maximization of the bandgap between the 3rd and 4th are the same as the 4th eigenfrequency maximization results. Figure 3.22 shows the optimized fiber angles and Figure 3.23 shows the convergence of this optimization process. The objective function begins at approximately 54 Hz and converges to about 170 Hz, over three times larger than the starting unidirectional bandgap. Table 3.3 presents the comparison between the optimization results and the ABAQUS results from the approximated optimized lay-up.

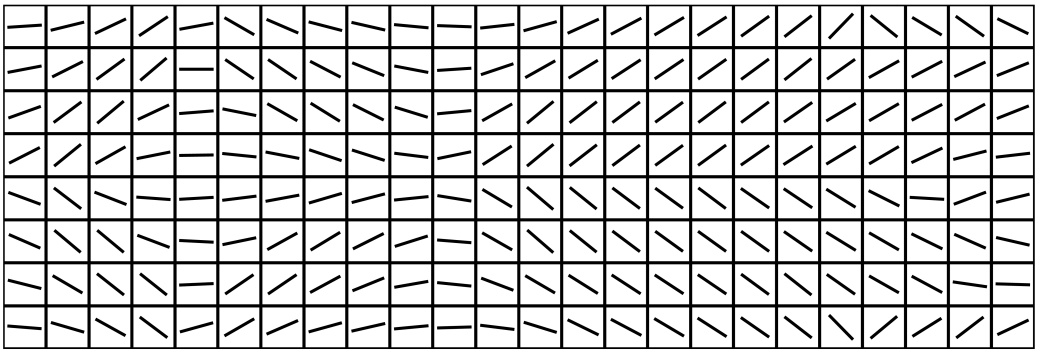

Figure 3.22: Results of optimization for maximization of the bandgap between the 3rd and 4th eigenfrequencies

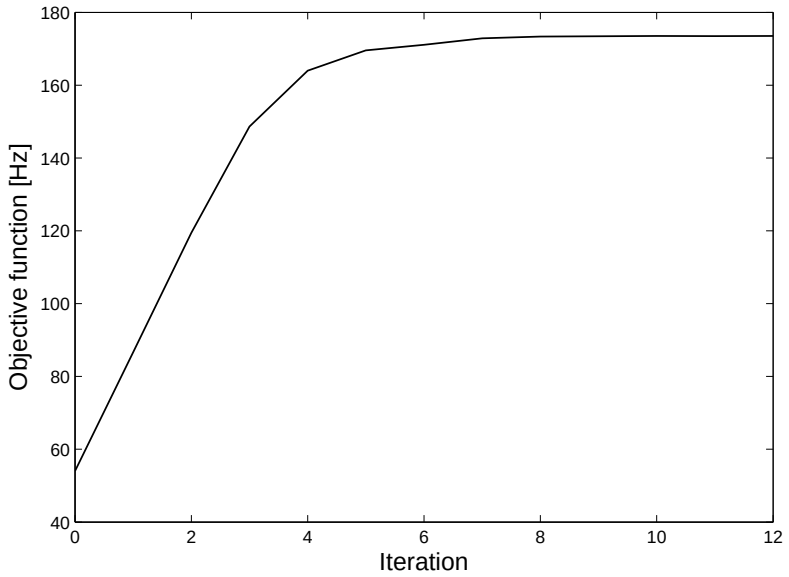

Figure 3.23: Convergence for the maximization of the bandgap between the 3rd and 4th eigenfrequencies

	Modes					
Description	1	2	3	4	5	6
Optimized	15.54	63.88	94.33	265.41	266.68	435.15
ABAQUS	15.69	62.80	101.43	271.27	273.06	440.19

Table 3.3: Eigenfrequencies calculated from optimized results from maximization of the 3rd and 4th eigenfrequencies

The results of the optimization for the maximization of the bandgap between the 4^{th} and 5^{th} eigenfrequencies are shown in Figures 3.24 and 3.25. In a similar manner to the $2-3$ bandgap optimization, the optimized fiber angles are largely unidirectional at $0°$. It can be seen on the convergence plot that the objective function increases from approximately 182 Hz to 205 Hz over 20 iterations. Table 3.4 presents the eigenfrequencies of the optimized plate as calculated from the optimization results and from the ABAQUS approximation and it can be seen that there are some noticeable differences between the results for the second, third and fifth modes. Like the discrepancy mentioned previously for the $1-2$ bandgap plate, the cause of these differences can also be attributed to the approximation process. The optimal ply for the $5-6$ bandgap maximization is the most complex of the results presented in this thesis and therefore the approximation process will have a larger affect on its eigenfrequencies than it would on the more basic optimal plies.

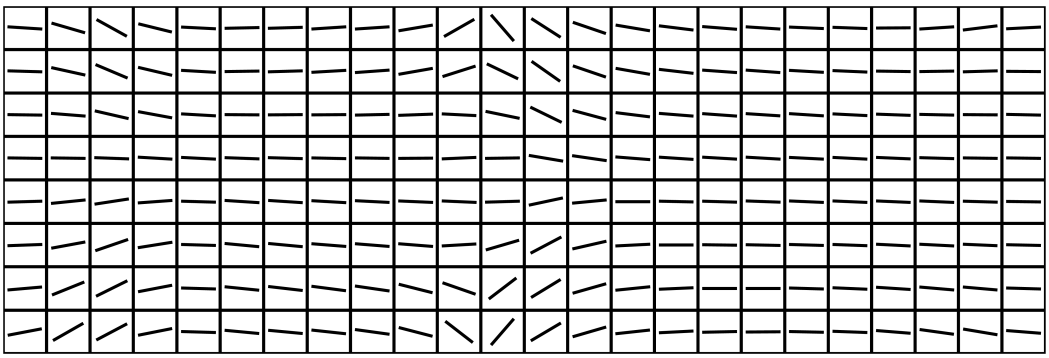

Figure 3.24: Results of optimization for maximization of the bandgap between the 4^{th} and 5^{th} eigenfrequencies

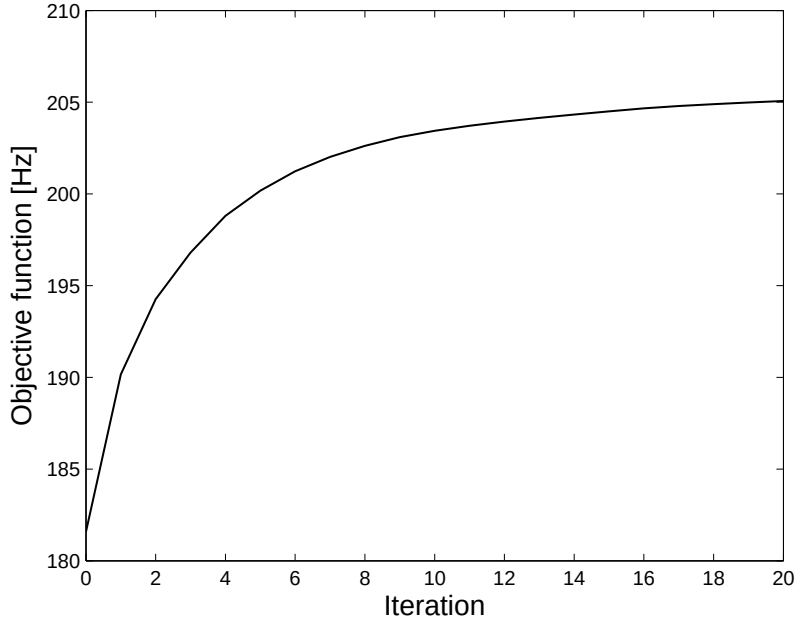

Figure 3.25: Convergence for the maximization of the bandgap between the 4^{th} and 5^{th} eigenfrequencies

	Modes					
Description	1	2	3	4	5	6
Optimized	19.28	50.77	114.58	157.87	363.02	384.56
ABAQUS	19.42	49.98	114.95	158.50	360.29	384.91

Table 3.4: Eigenfrequencies calculated from optimized results from maximization of the 4^{th} and 5^{th} eigenfrequencies

The maximization of the $5-6$ bandgap begins at approximately 18 Hz and increases to around 224 Hz after 21 iterations. The optimized fiber angles are shown in Figure 3.26 and the convergence of the objective function can be seen in Figure 3.26. The comparison of the optimization results and the ABAQUS approximation is presented in Table 3.5. Comparing these results with the previous few sets it is clear that the optimal fiber angles for maximizing the $5-6$ bandgap are more complex. This can also be observed in the ABAQUS calculations which show a larger difference from the optimization results than

the other bandgap optimizations.

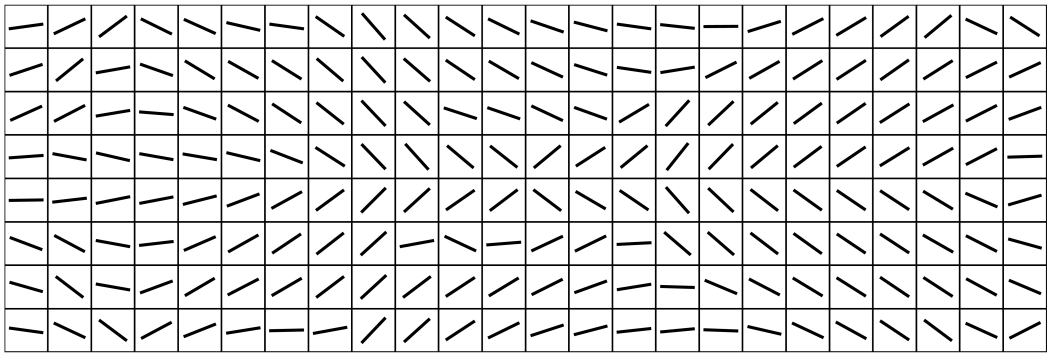

Figure 3.26: Results of optimization for maximization of the bandgap between the 5$^{\text{th}}$ and 6$^{\text{th}}$ eigenfrequencies

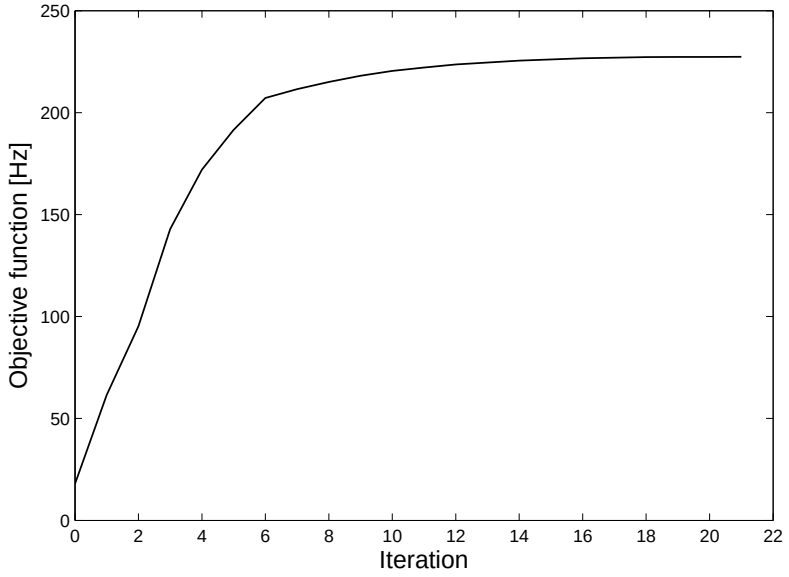

Figure 3.27: Convergence for the maximization of the bandgap between the 5$^{\text{th}}$ and 6$^{\text{th}}$ eigenfrequencies

	Modes					
Description	1	2	3	4	5	6
Optimized	16.15	69.72	97.85	225.12	261.38	484.86
ABAQUS	17.80	58.34	110.16	226.13	300.71	484.25

Table 3.5: Natural frequencies [Hz] calculated for the optimal fiber angles for the maximization of the bandgap between the 5$^{\text{th}}$ and 6$^{\text{th}}$ eigenfrequencies

3.2.3 Other Eigenfrequency Gaps

In addition to the single eigenfrequency and bandgap optimization, the fiber angles were optimized to maximize the gap between arbitrary eigenfrequencies for informational purposes. Presented below are the resulting optimized fiber angles and the plots of their convergence.

The gap between the first and third eigenfrequencies does not change much throughout the optimzation process, as shown in Figure 3.28. This is due to the fact that the maximized fiber angles for the single eigenfrequencies are nearly identical (fully unidirectional).

The resulting optimized fiber angles for the $1-4$ and $2-4$ gaps are nearly identical to each other and to the results from the $3-4$ bandgap and the fourth eigenfrequency maximization. The results from the $1-4$ gap optimization are shown in Figure 3.29 and the $2-4$ gap results are in Figure 3.30. Both sets of results show a large improvement over the unidirectional starting condition.

The results from the optimization for the first two gaps, $1-5$ and $2-5$, show minimal improvement from the unidirectional starting condition. However, the maximization of the $3-5$ gap shows some improvement increasing from approximately 236 Hz to 264 Hz over 32 iterations. The results for these optimizations are presented in Figures 3.31 - 3.33.

Unlike the previous sets of optimizations, the results for maximizing gaps using the sixth eigenfrequency provide several unique ply designs. The results for the maximization of the $1-6$ gap are shown in Figure 3.34. The objective function increases from approximately 365 Hz to 495 Hz following an atypical convergence path. Figure 3.35 presents the outcome of maximizing the $2-6$ gap. It went from approximately 335 Hz

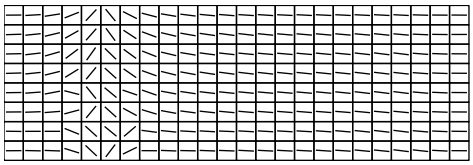

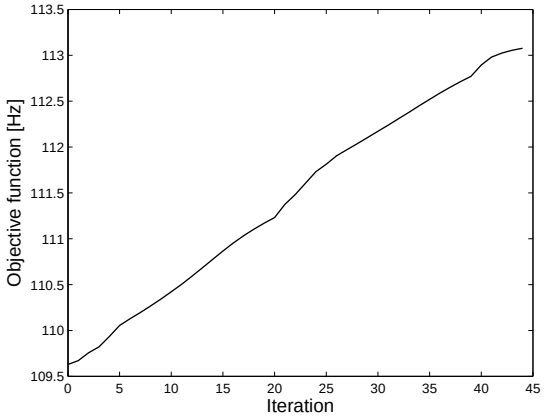

(a) Optimized fiber angles (b) Convergence

Figure 3.28: Optimization results for the maximization of the $1-3$ gap

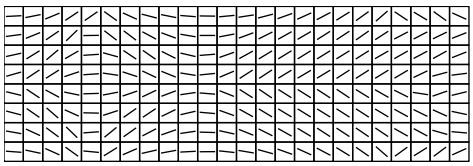

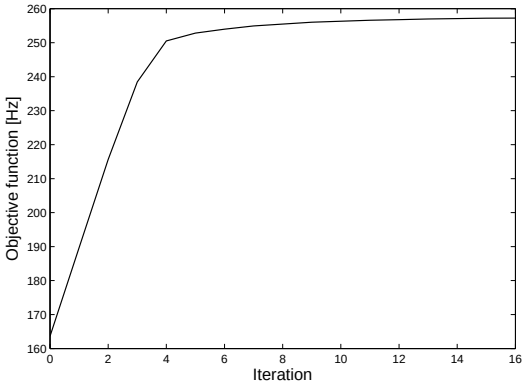

(a) Optimized fiber angles (b) Convergence

Figure 3.29: Optimization results for the maximization of the $1-4$ gap

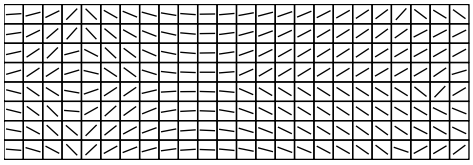

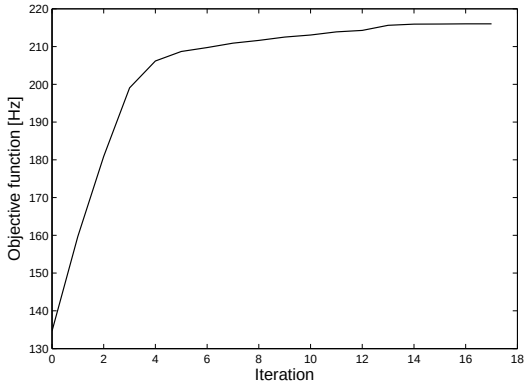

(a) Optimized fiber angles (b) Convergence

Figure 3.30: Optimization results for the maximization of the $2-4$ gap

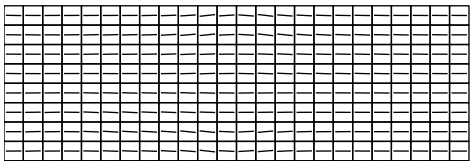

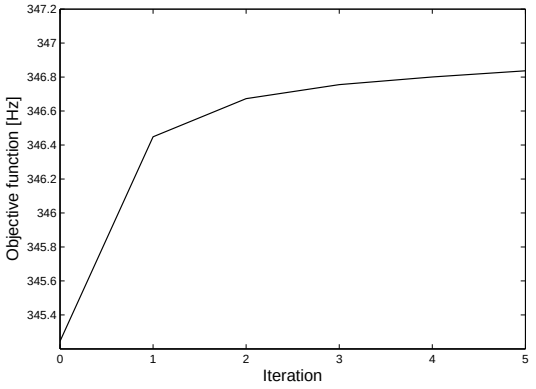

(a) Optimized fiber angles (b) Convergence

Figure 3.31: Optimization results for the maximization of the $1-5$ gap

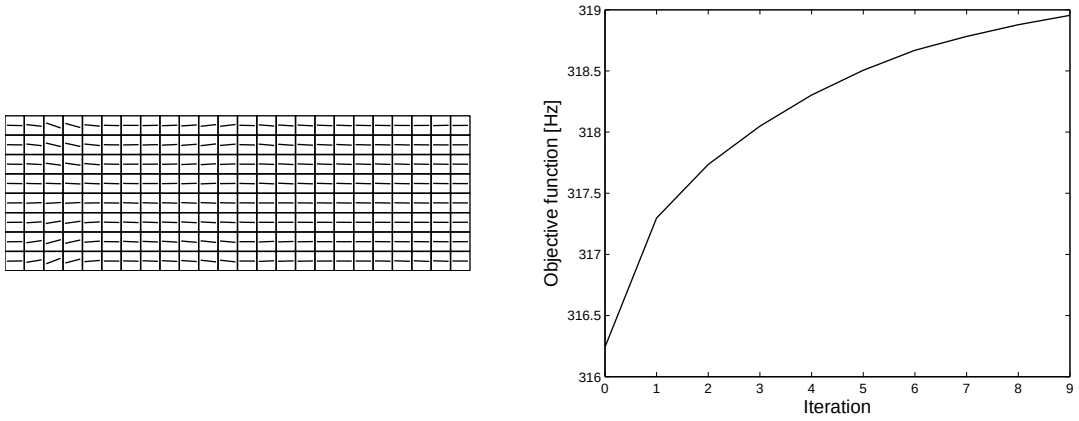

(a) Optimized fiber angles (b) Convergence

Figure 3.32: Optimization results for the maximization of the $2-5$ gap

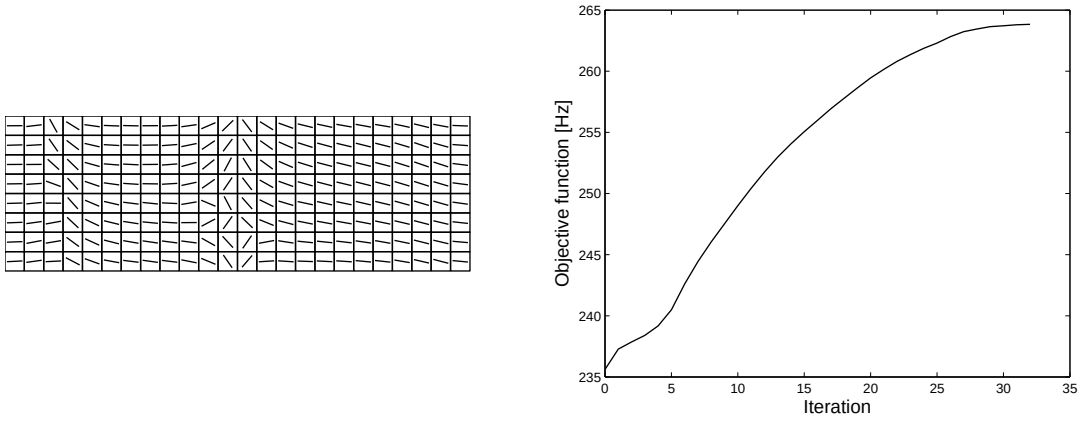

(a) Optimized fiber angles (b) Convergence

Figure 3.33: Optimization results for the maximization of the $3-5$ gap

to 390 Hz.

The optimized fiber angles for the $3-6$ gap, seen in Figure 3.36, are similar to the results from the $1-6$ gap maximization. The objective function starts at approximately 255 Hz and increases to about 410 Hz after 22 iterations. The results for the $4-6$ gap optimization are shown in Figure 3.37. Its objective function increases by 60 Hz in 29 iterations, starting from around 200 Hz.

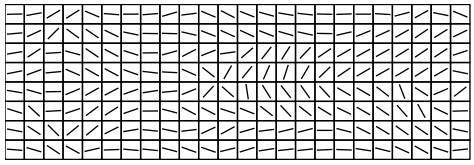

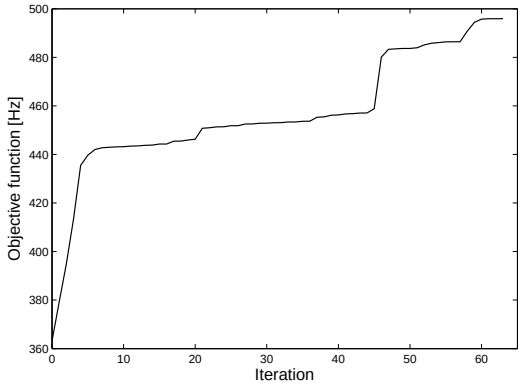

(a) Optimized fiber angles (b) Convergence

Figure 3.34: Optimization results for the maximization of the $1-6$ gap

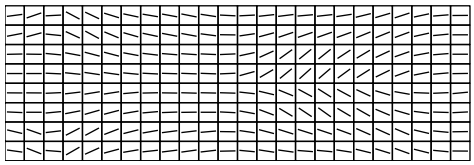

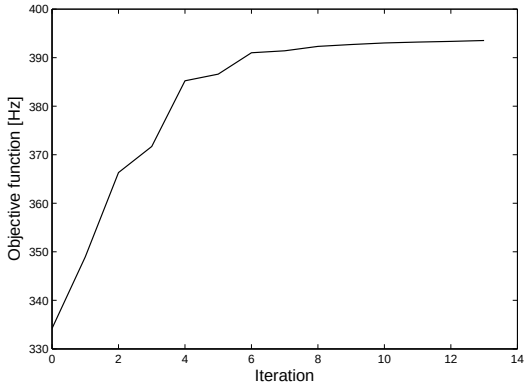

(a) Optimized fiber angles (b) Convergence

Figure 3.35: Optimization results for the maximization of the $2-6$ bandgap

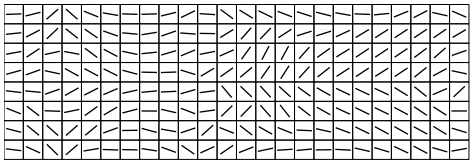

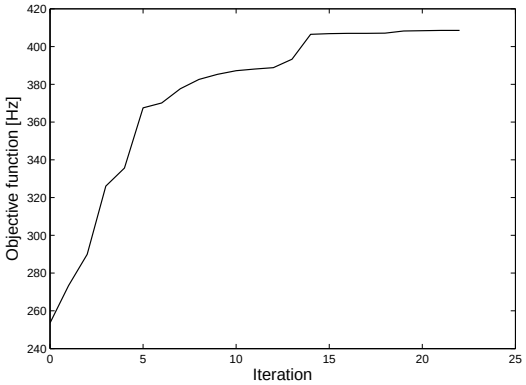

(a) Optimized fiber angles (b) Convergence

Figure 3.36: Optimization results for the maximization of the $3-6$ bandgap

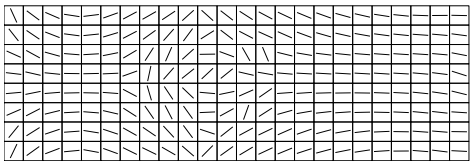

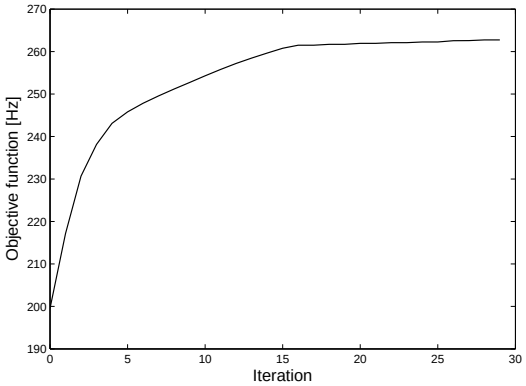

(a) Optimized fiber angles (b) Convergence

Figure 3.37: Optimization results for the maximization of the $4-6$ bandgap

Chapter 4

Modal Analysis

To validate the results presented in the previous chapter, the optimized laminated composite plates were fabricated from unidirectional prepreg carbon fiber tape and subjected to modal testing. In conjunction with the modal testing, commercial FEA software was used to determine the vibrational characteristics of the optimized plates, and to also ensure that there were no errors in the optimization results before plate fabrication had begun. This chapter presents the results of the modal analysis of the plates along with an overview of the fabrication and testing procedures used.

4.1 Testing Procedure

As mentioned previously in Chapter 2, the hardware used in the modal testing is an impact hammer for excitation and an accelerometer for measuring the response. Both were purchased from PCB Piezotronics Inc; the hammer is model 086C01 and the accelerometer is model 352A24. The accelerometer and impact hammer are shown in Figure 4.2. The data aquisition and signal conditioning were performed with a National Instruments signal conditioner, SC-2354, with two SCC-ACC01 Accelerometer input modules, connected to a computer with Labview software. The Labview interface created for the modal analysis samples the inputs from the input modules at a user specified sampling

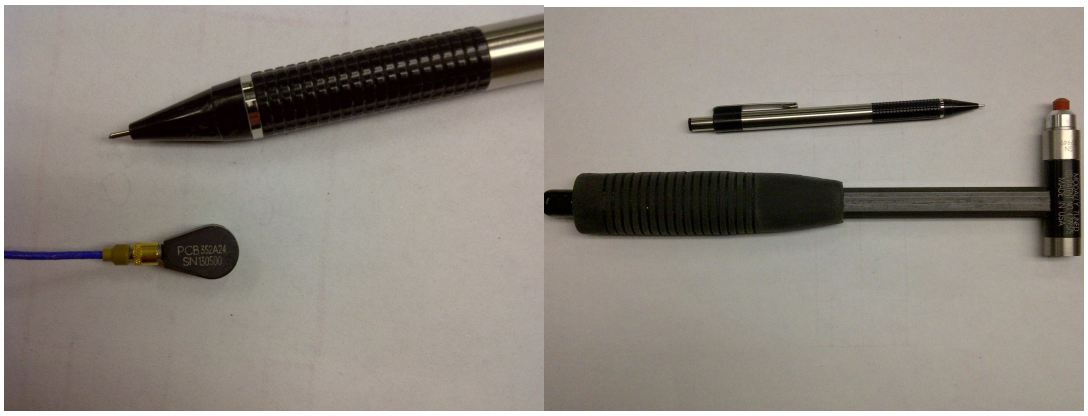

(a) Accelerometer (b) Impact Hammer

Figure 4.2: Modal testing hardware shown with a pencil for scale

frequency and writes the values to a spreadsheet. These are the time-domain values which are analyzed as stated in Chapter 2. The Labview block diagram is shown in Figure 4.1.

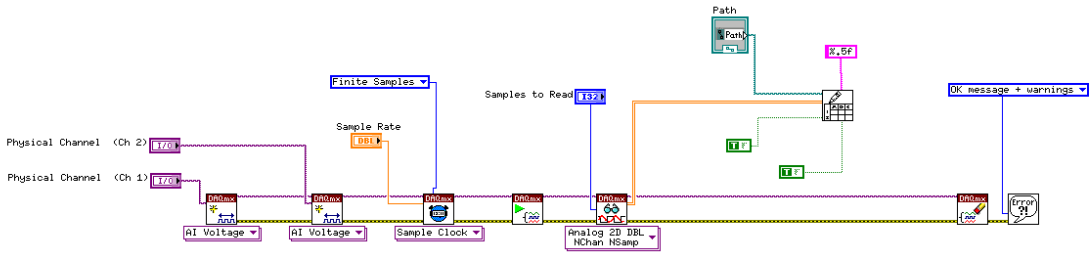

Figure 4.1: Labview block diagram for reading modal analysis data and saving to a file

The general procedure for performing the modal testing is straightforward. The accelerometer is attached to a specific point on the plate with wax and the impact hammer is used to provide an impulse at a certain location, and ten measurements are taken to ensure high quality data is recorded and to allow for the averaging of results. The location of the accelerometer and hammer strikes were rotated through several different locations

in an effort to capture all relevant modes of vibration. To impose the cantilevered boundary condition one end of the plate is clamped in a table clamp. A cantilevered plate with accelerometer attached can be seen in Figure 4.3.

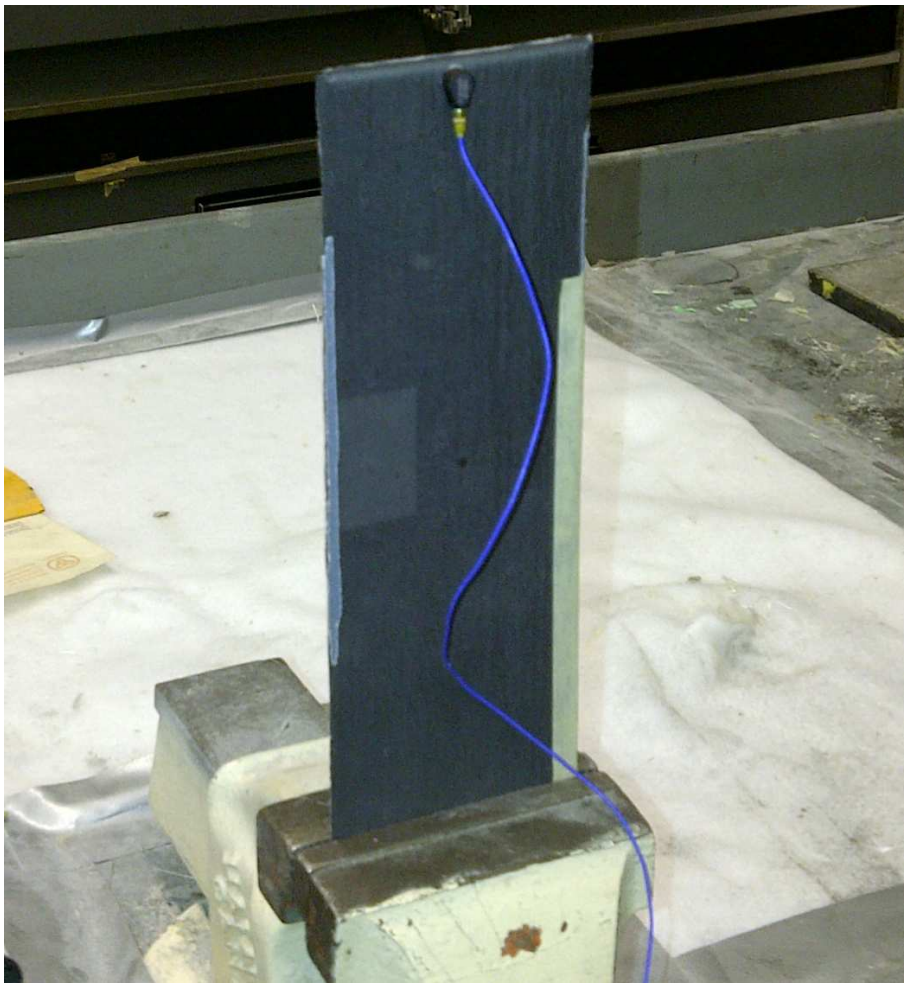

Figure 4.3: Accelerometer attached to plate ready for testing

4.2 Fabrication

To lay up the optimized plies by hand the optimization results have to be converted to a simpler design while still maintaining the vibrational characteristics of the optimized results. This is accomplished by grouping fiber angles with similar surrounding fibers to produce larger unidirectional "patches". An example of a plate constructed from these unidirectional patches can be seen in Figure 4.4.

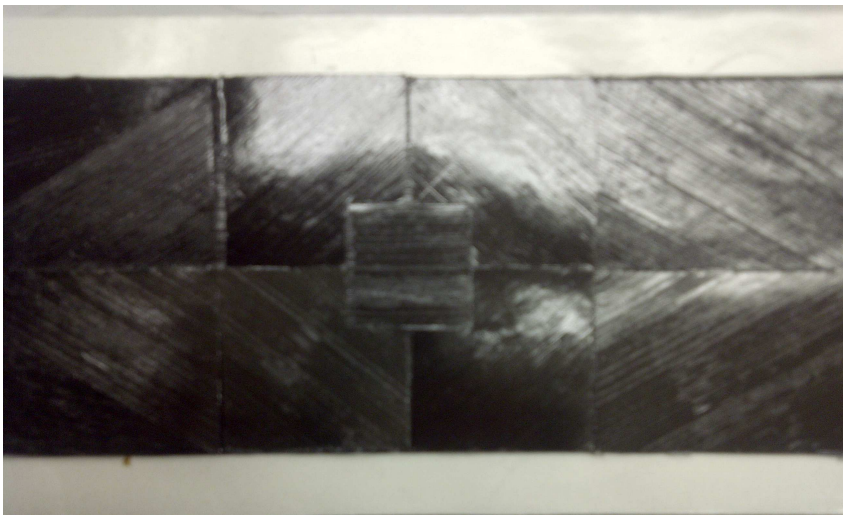

Figure 4.4: Lay-up of an optimized ply for the maximization of the 2^{nd} eigenfrequency

The plates were first made with the same 5-ply lay-up configuration as used for the optimization process, [opt, 0°, o$\bar{\text{p}}$t]$_s$, where "opt" refers to a ply composed of the optimal local fiber angles, but a problem was encountered when the plates warped during the curing process. Due to the orthotropic properties of the material and the optimized plies, certain areas of the plate will contract more than the others upon curing, creating a warp in the plate and thus preventing it from undergoing modal testing. Several potential solutions were attempted, such as modifying the lay-up configurations to [opt, 0°, $\bar{0}$°]$_s$ or [opt, 0°, 9$\bar{0}$°]$_s$ and using a heavy flat plate on top of the bagged plate during curing. Unfortunately none of these solutions were able to entirely remove the warping, so additional plies had to be added to increase the thickness of the plate. The following 10-ply lay-up configuration was used for the modal testing: [opt, 0°, opt, 90°, $\bar{0}$°]$_s$. By doubling the number of plies, the warping was eliminated.

4.3 Results

In this section the results from the modal testing are presented along with ABAQUS calculations for the 10-ply plates. Calculations were performed in ABAQUS uing two dif-

ferent versions of the optimized ply; one being the regular optimization results (corrected for symmetry and angles rounded to nearest multiple of five) and the other being the approximated hand lay-up version on which the plate fabrication was based on. The results of the modal testing are presented as plots of the frequency response function measured at two different locations: the top-center and top-right corner of the cantilevered plate. Additionally, the eigenfrequencies as calculated by ABAQUS for the approximated lay-up version of the plate are plotted as vertical lines over the FRF plot to allow for an easy comparison of experimental and theoretical results.

The results of the modal testing of the plate optimized for the maximization of the $1-2$ bandgap are presented in Figures 4.5 and 4.6. From both figures it can be seen that the first three eigenfrequencies in the frequency response function (FRF) match their respective predicted values which are presented in Table 4.1. As the mode number increases, some divergence is seen in the predicted and experimental eigenfrequencies. The fourth and fifth predicted eigenfrequencies fall on either side of a peak in the FRF and the sixth eigenfrequency of the FRF was found to be either slightly lower or higher than the predicted value based on the placement of the accelerometer.

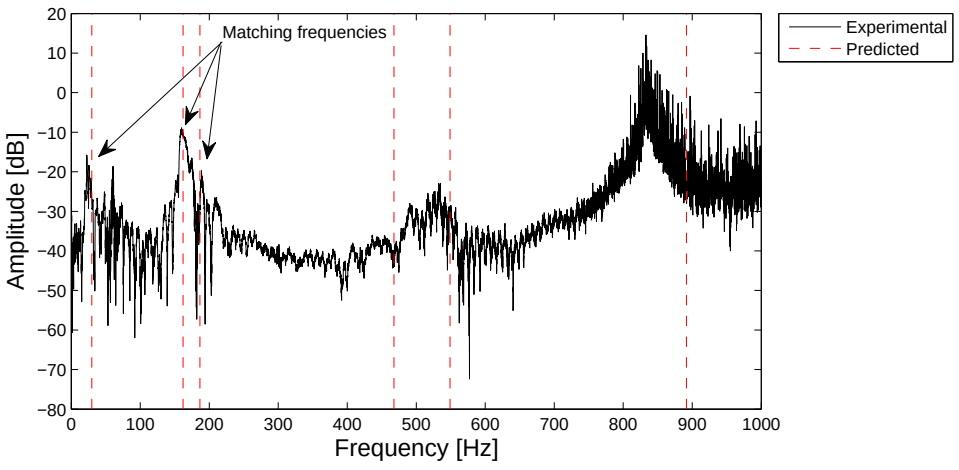

Figure 4.5: Frequency response funtion calculated from the accelerometer attached to the top-center of the plate with a maximized $1-2$ bandgap

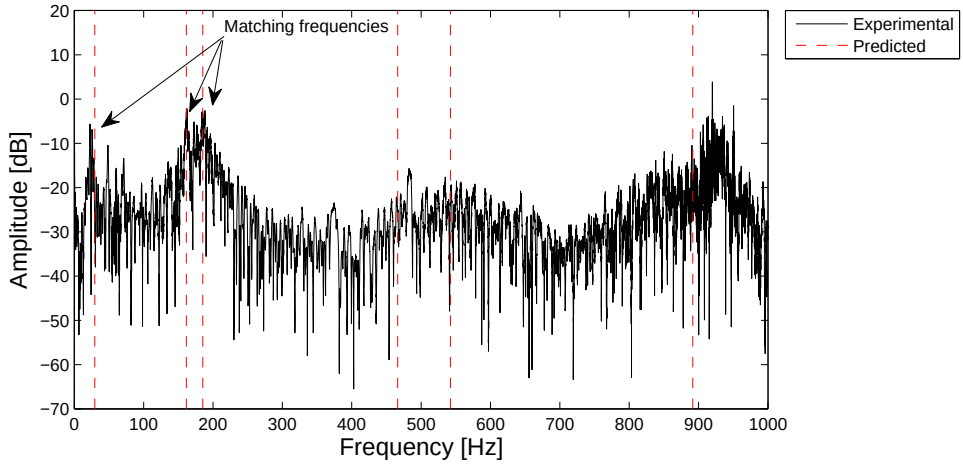

Figure 4.6: Frequency response funtion calculated from the accelerometer attached to the top-right corner of the plate with a maximized $1-2$ bandgap

	Modes					
Description	1	2	3	4	5	6
Optimized	31.02	164.75	194.86	474.46	564.31	910.59
Layup	29.70	161.51	185.23	466.31	542.24	891.67

Table 4.1: Predicted results from ABAQUS calculations for the $1-2$ bandgap maximization

The experimental results of the $2-3$ bandgap plate show little correlation with the predicted eigenfrequencies. One possible reason is the fact that the optimized ply is fully unidirectional with the fibers all oriented at $0°$ from horizontal; this creates an incredibly stiff plate in bending and therefore the amplitude and the length of the induced vibrations are very small. The first three predicted eigenfrequencies are close to peaks of the FRF in Figure 4.7. The first and third eigenfrequencies match up well with a small and large peak, respectively, on both FRF plots, while the predicted second eigenfrequency lies between two small peaks in Figure 4.7. The remaining sets of eigenfrequencies do not match up at all. Since the optimized ply was very similar to a unidirectional ply, the eigenfrequencies were calculated for the lay-up only. The predicted eigenfrequencies can

be found in Table 4.2.

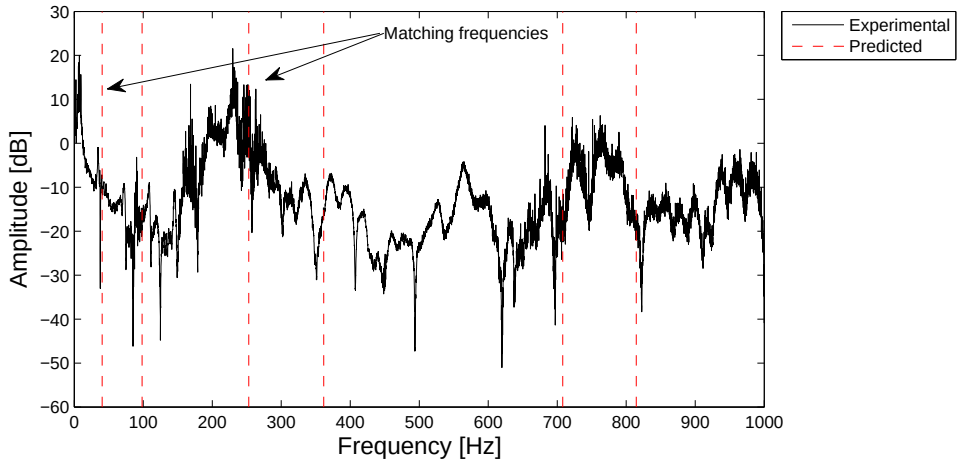

Figure 4.7: Frequency response funtion calculated from the accelerometer attached to the top-center of the plate with a maximized $2-3$ bandgap

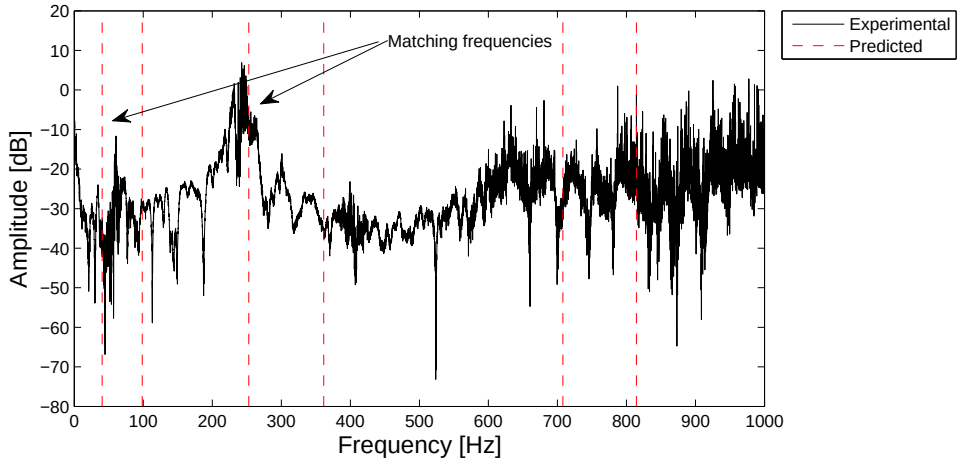

Figure 4.8: Frequency response funtion calculated from the accelerometer attached to the top-right corner of the plate with a maximized $2-3$ bandgap

	Modes					
Description	1	2	3	4	5	6
Layup	40.39	98.44	252.91	361.48	707.93	814.52

Table 4.2: Predicted results from ABAQUS calculations for the $2-3$ bandgap maximization

The testing results of the plate optimized for the maximization of the bandgap between the third and fourth eigenfrequencies are shown in Figures 4.9 and 4.10. The predicted first, third and sixth eigenfrequencies correspond well to the experimental data, each on (or very near) a peak in at least one of the FRFs. The fourth and fifth predicted eigenfrequencies fall on either side of a wide peak in Figure 4.9, while no peak in the FRF is present for the second eigenfrequency. The calculated eigenfrequencies are shown in Table 4.3.

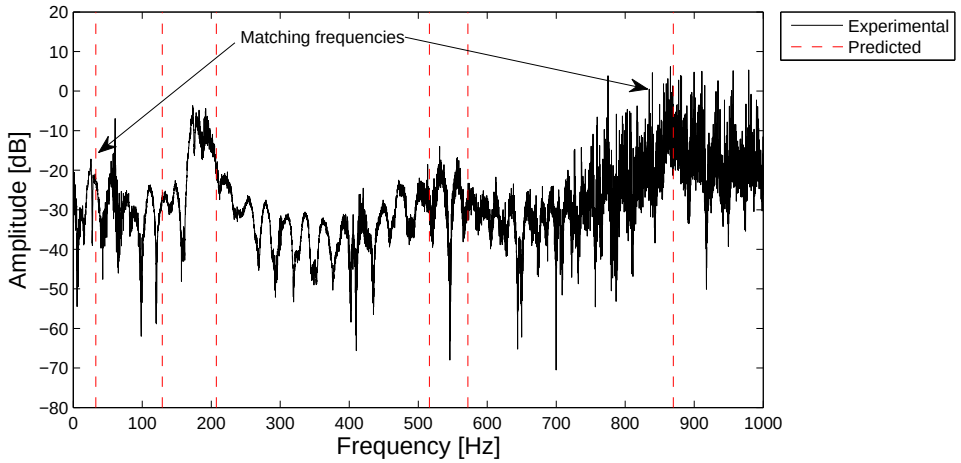

Figure 4.9: Frequency response funtion calculated from the accelerometer attached to the top-center of the plate with a maximized $3-4$ bandgap

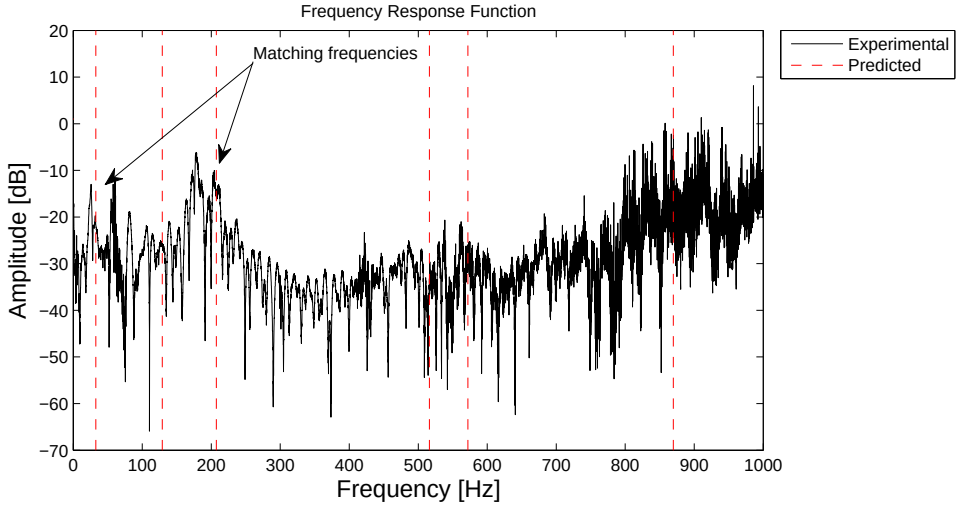

Figure 4.10: Frequency response funtion calculated from the accelerometer attached to the top-right corner of the plate with a maximized $3-4$ bandgap

	Modes					
Description	1	2	3	4	5	6
Optimized	33.16	124.85	213.93	523.61	579.20	879.99
Layup	33.04	131.85	206.12	513.54	567.05	868.37

Table 4.3: Predicted results from ABAQUS calculations for the $3-4$ bandgap maximization

Figures 4.11 and 4.12 show the test results for the $4-5$ bandgap optimized plate. As with the previous plate, the first, third, and sixth predicted eigenfrequencies match up well with their experimental values and the predicted second eigenfrequency does not correspond to any peak on the FRF. With the accelerometer placed in the top-right corner of the plate a peak which is near the predicted fourth eigenfrequency appears in the FRF. In addition, Figure 4.11 has peak in the FRF in the vicinity of the fifth eigenfrequency, demonstrating that accelerometer placement has an effect on the observed frequencies. The calculated eigenfrequencies are presented in Table 4.4.

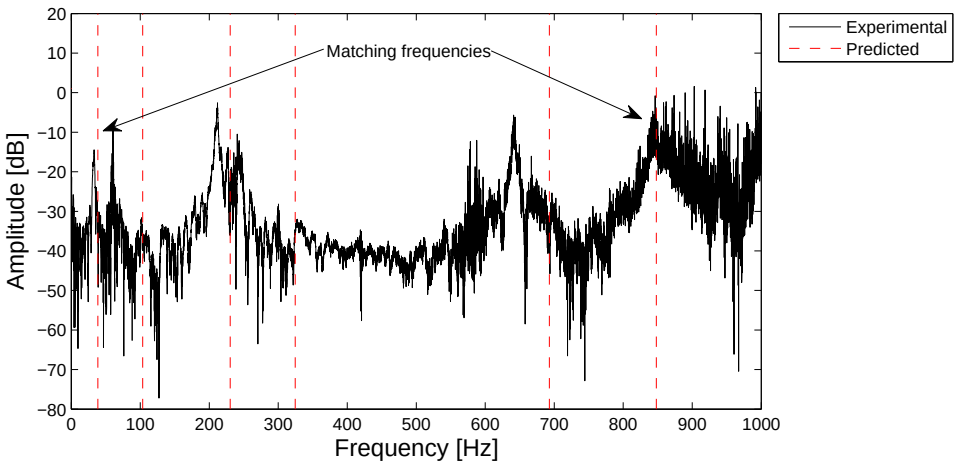

Figure 4.11: Frequency response funtion calculated from the accelerometer attached to the top-center of the plate with a maximized $4-5$ bandgap

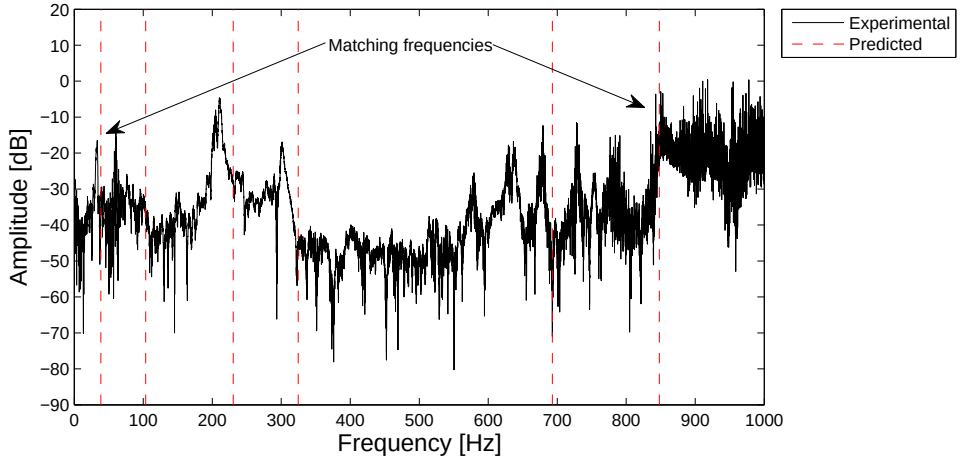

Figure 4.12: Frequency response funtion calculated from the accelerometer attached to the top-center of the plate with a maximized $4-5$ bandgap

	Modes					
Description	1	2	3	4	5	6
Optimized	38.54	100.37	232.43	323.80	702.84	846.53
Layup	38.58	103.49	230.42	324.49	692.87	847.93

Table 4.4: Predicted results from ABAQUS calculations for the $4-5$ bandgap maximization

The final plate tested was the one optimized for the maximization of the $5-6$ bandgap. The results are presented in Figures 4.13 and 4.14. The first and third predicted eigenfrequencies match up well with peaks in the FRF in both plots, but, like previouisly, there is no peak in the FRF near the second eigenfrequency. When the accelerometer is placed at the top-center of the plate the fourth and fifth eigenfrequencies are on either side of a peak in the FRF; with the accelerometer placed in the top-right corner the peak in the FRF moves to a frequency slightly higher than the predicted fifth frequency. Looking at the sixth eigenfrequency, the predicted value is slightly higher in frequency than the peak in the FRF, with the FRF in Figure 4.14 being closer to the predicted than the FRF in Figure 4.13. The calculated eigenfrequencies are located in Table 4.5.

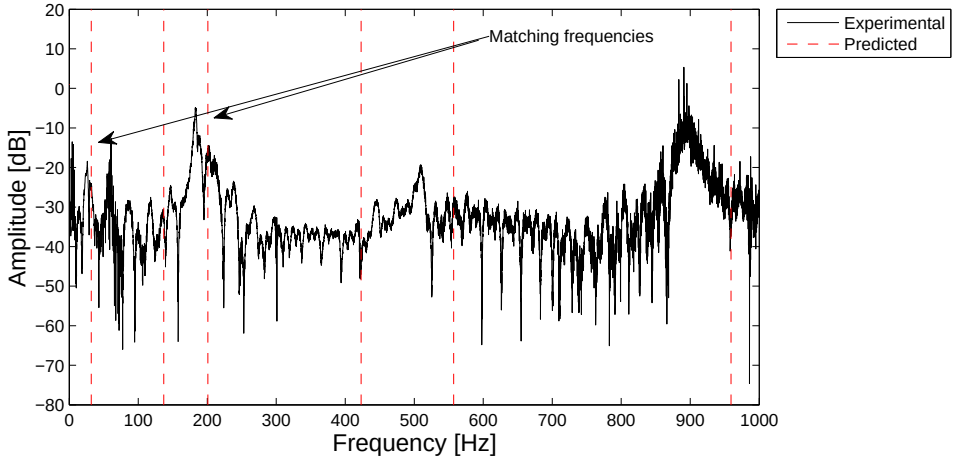

Figure 4.13: Frequency response funtion calculated from the accelerometer attached to the top-center of the plate with a maximized $5-6$ bandgap

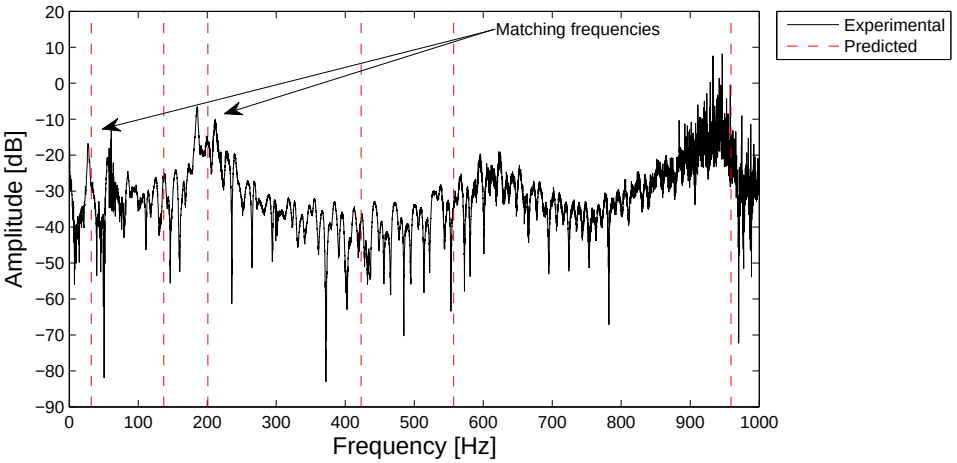

Figure 4.14: Frequency response funtion calculated from the accelerometer attached to the top-right corner of the plate with a maximized $5-6$ bandgap

	Modes					
Description	1	2	3	4	5	6
Optimized	33.28	138.94	204.88	447.96	562.19	958.80
Layup	31.87	136.96	200.98	423.12	557.10	959.11

Table 4.5: Predicted results from ABAQUS calculations for the $5-6$ bandgap maximization

Overall, the frequency response functions aligned with around half of the predicted eigenfrequencies while also sometimes having peaks near the other predicted values. It was also noticed that for the majority of the optimized plates the second predicted eigenfrequency did not line up with the observed results. When this was the case the FRF would have a peak in between the first and second eigenfrequencies. A possible cause for this could be the placement of the accelerometer; its current locations may not have been in a region with a large amount of amplitude. Another interesting observation is that the bandgaps which were the focus of the observation are easily visible when viewing the plotted predicted eigenfrequencies. While all of the bandgaps vary in size, the maximized one is clearly the largest and easily spotted.

Chapter 5

Conclusions

This thesis presents a method for optimizing the local fiber orientations in thin composite plates to maximize specific eigenfrequencies and eigenfrequency bandgaps. This optimization process can be useful when confronted with the need to maximize the performance of a geometrically constrained composite component. The orthotropic nature of the mechanical properties of carbon fiber are taken advantage of to produce a part using the most efficient use of material possible.

The composite plates were modelled using First Order Shear Deformation Theory which assumes the laminated plate is a single layer with complex constitutive behaviour. When the plates are discretized, each element will have a set of fiber angles corresponding to each ply. Prior to the optimization process it has to be dedcided which plies to optimize. The Steepest Descent Method was used to conduct the optimization, the sensitivities were calculated using a simple finite difference approximation, and the optimal step size was determined using the golden section search method. The optimization process was performed on cantilevered rectangular plates which had an aspect ratio of 3:1.

In the single eigenfrequency maximization case, it was shown that the optimization process will provide a significant increase in the targeted eigenfrequency over the unidirectional starting condition. In addition, viewing the optimized fiber angles and the vibration mode shape next to each other allows for a greater understanding of their relationship. When maximizing eigenfrequency bandgaps the optimal fiber orientations are often very similar to the results from the single eigenfrequency maximization for the larger eigenfrequency in the bandgap (i.e. the results from the $1-2$ bandgap maximization are the same as the results from the 2^{nd} eigenfrequency maximization). As the mode numbers of the bandgap increase, the similarity between the bandgap and single eigenfrequency maximization results is reduced; this begins for the $4-5$ eigenfrequency bandgap. Generally, a large increase in the targeted bandgap was observed during the optimization process. The exception to this were the $2-3$ and $4-5$ bandgaps and the other arbitrary gaps with 3 or 5 as the larger of the two frequencies. Since these gaps and bandgaps had an odd eigenfrequency as the dominant frequency of the pair their optimal fiber orientations are heavily unidirectional which is the starting condition.

To validate the results from the optimization process the optimal fiber orientations were converted into an approximate lay-up and 10-ply laminated composite plates, $[\text{opt}, 0^\circ, \text{opt}, 90^\circ, \bar{0}^\circ]_s$, were fabricated for modal testing. The modal testing was conducted using an accelerometer, attached to the plate with wax, and an impact hammer, to provide excitation. The instrumentation was controlled with Labview and the data was analyzed in Matlab.

The results of the modal testing can be found in Section 4.3. The vibration was recorded at the top-center and top-right corners of the plates. One observation from the figures of the results is that the higher eigenfrequencies are both more difficult to measure and more difficult to control. The FRF plots rarely had any prominent peaks for the fourth and fifth eigenfrequencies while the sixth eigenfrequency sometimes had

a peak (which may or may not have been near the predicted sixth eigenfrequency). On the other hand the first and third eigenfrequencies ususally had the predicted values near the experimental results. The second eigenfrequency had more unique results; there was always a prominent peak in the FRF plot but it was usually not near the predicted value. Only the results from the $1-2$ bandgap have matching predicted and experimental second eigenfrequencies.

The optimization results presented in Secton 3 demonstrated the feasibility of optimizing the orientation of orthotropic material for the maximization of eigenfrequency bangaps. The results in this section were also verified with commercial FEA software. Fabricating the optimized plates and subjecing them to modal testing demonstrated that the increased bandgap size does carry over from the theoretical calculations. A great example of this are the $1-2$ bandgap maximization results. However, it was also observed that as the mode numbers increase so does the difficulty of fabricating the optimized fiber layout, and therefore it is more difficult to maintain the predicted vibrational characteristics. A more accurate method of fabrication may be required for the more complicated optimized designs, which will be discussed in more detail in the next section, along with other recommendations.

5.1 Recommendations

There are several ways in which the optimization process can be improved. The change to the optimization algorithm that will yield the greatest results in terms of efficiency is to use the adjoint method to calculate the sensitivities in place of the current finite difference method, as seen in [13] and [6]. With the adjoint method, the eigenvalues do not need to be recalculated for every design variable (fiber angle); instead only the stiffness matrix needs to be recalculated and this is a much quicker process. Another improvement in the calculation speed can be made by using an algorithm that is more suitable for solving

the general eigenproblem with large symmetric positive definite matrices. Currently QR decomposition is used, but using an algorithm such as the Lanczos method or subspace iteration should improve the calculaton speed [4]. A quicker eigenproblem solving algorithm will have a large impact on the speed of the step size line search portion of the optimizaion process since the eigenvalues need to be calculated in every iteration of the line search. Lastly, the optimization algorithm itself should be considered for improvement. Currently the steepest descent method is used; it is simple but slow. One option would be to use the Method of Moving Asymptotes (MMA) as described by [20] and [21], and used in [13] and [5] among others. More efficient optimization methods can reduce the number of iterations required before a convergence to a solution and also decrease the time required per iteration.

One aspect of composite design that was not considered in the optimization process is manufacturability. The fiber angles of adjacent elements are unrestricted and therefore the optimized designs could create some difficulties in their fabrication, even when using technologies such as advanced tow placement. To incorporate manufacturability into the optimization process one could impose constraints on fiber angles to ensure that the results are viable or possibly employ some form of post-processing on the results to create a manufacturable final product.

To get optimized results that are more forgiving for hand lay-up a different approach may have to be taken. Discrete material optimization (DMO) is a method that is very similar topology optimization with multiple materials. In the place of the multiple different materials that topology optimization would use, DMO will have an orthotropic material defined at many different angles (i.e. $0°, \pm 15°, \pm 30°$, etc). DMO also employs the Solid Isotropic Material with Penalization (SIMP) approach and can be solved using MMA [19][7]. In addition to the fixed angles which make the hand lay-up process simpler, DMO can also use patch variables to group many elements together to act as one, which

resemble patches of unidirectional prepreg tape.

Bibliography

[1] Gnu scientific library. http://www.gnu.org/software/gsl/.

[2] Open mpi. http://www.open-mpi.org/.

[3] Openmp. http://openmp.org/wp/.

[4] K. Bathe. *Finite Element Procedures in Engineering Analysis*. Prentice-Hall, Inc., 1982.

[5] A. Larsen et al. Topological material layout in plates for vibration suppression and wave propagation control. *Structural and Multidisciplinary Optimization*, 37:585–594, 2009.

[6] A. P. Seyranian et al. Multiple eigenvalues in structural optimization problems. *Structural and Multidisciplinary Optimization*, 8:207–227, 1994.

[7] B. Niu et al. Discrete material optimization of vibrating laminated composite plates for minimum sound radiation. *International Journal of Solids and Structures*, 47:2097–2114, 2010.

[8] D. Ewins. *Modal Testing*. Research Studies Press, 2000.

[9] A. J. M. Ferreira. *MATLAB Codes for Finite Element Analysis*. Springer, 2009.

[10] Du Jianbin and Niels Olhoff. Topological design of freely vibrating continuum structures for maximum values of simple and multiple eigenfrequencies and frequency band gaps. *Structural and Multidisciplinary Optimization*, 34:91–110, 2007.

[11] R. Jones. *Mechanics of Composite Materials*. Taylor and Francis, 1999.

[12] N. L. Pedersen. Maximization of eigenvalues using topology optimiaztion. *Structural and Multidisciplinary Optimization*, 20:2–11, 2000.

[13] N. L. Pedersen. Designing plates for minimum internal resonances. *Structural and Multidisciplinary Optimization*, 30:297–307, 2005.

[14] J. N. Reddy. *Mechanics of Laminated Composite Plates and Shells, Theory and Analysis*. CRC Press, 2004.

[15] O. Sigmund. A 99 line topology optimization code written in matlab. *Structural and Multidisciplinary Optimization*, 21:120–127, 2001.

[16] O. Sigmund and S. Torquato. Design of materials with extreme elastic or thermoelastic properties using topology optimization. *IUTAM Symposium on Transformation Problems in Composite and Active Materials*, pages 233–244, 1998.

[17] O. Sigmund and S. Torquato. Design of smart composite materials using topology optimization. *Smart Materials and Structures*, 8:365–379, 1998.

[18] Ole Sigmund. On the design of compliant mechanisms using topology optimization. *Mechanics Based Design of Structures and Machines*, 25:493–524, 1997.

[19] J. Stegmann and E. Lund. Discrete material optimization of general composite shell structures. *International Journal for Numerical Methods in Engineering*, 62:2009–2027, 2005.

[20] K. Svanberg. The method of moving asymptotes - a new method for structural optimization. *International Journal for Numerical Methods in Engineering*, 24:359–373, 1987.

[21] C. Zillober. A globally convergent version of the method of moving asymptotes. *Structural and Multidisciplinary Optimization*, 6:166–174, 1993.